The Whakamaru Magmatic System (Taupō Volcanic Zone, New Zealand), Part 2: Evidence from ignimbrite deposits for pre-eruptive distribution of melt-dominated magma and magma mushes in the crust

Harmon, Lydia J, *ljharmo1@asu.edu, ORCID 0000-0002-9985-705X, Department of Earth & Environmental Sciences, Vanderbilt University, 2301 Vanderbilt Place, Nashville, TN 37235, USA and School of Earth and Space Exploration, Arizona State University, 781 Terrace Mall, Tempe, AZ 85287, USA

Smithies, Sarah L, School of Earth and Environment, University of Canterbury, Private Bag 4800, Christchurch 8140, New Zealand. ORCID 0000-0002-7734-2952

Gualda, Guilherme A R, Department of Earth & Environmental Sciences, Vanderbilt University, 2301 Vanderbilt Place, Nashville, TN 37235, USA. ORCID 0000-0003-0720-2679

Gravley, Darren M, School of Earth and Environment, University of Canterbury, Private Bag 4800, Christchurch 8140, New Zealand. ORCID 0000-0003-4451-9210

ABSTRACT

The Whakamaru volcanic deposits in Aotearoa New Zealand make up the largest eruptions in the young Taupō Volcanic Zone (TVZ). The complex volcanology and petrology of the multiple mappable ignimbrite units have obscured the number of eruptive phases, the relative timing of these eruption(s), and the pre-eruptive conditions of the magma bodies. To address these complexities, we use pumice clasts from multiple ignimbrite localities in conjunction with tephra deposits (Harmon et al., Part 1). Analysis of whole-rock and glass compositions from individual pumice clasts reveals the different magma types that participated in the eruptions. We confirm four main types of magma (types A, B, C, D; originally identified by Brown et al., 1998), which likely represent independent magma bodies. By examining the distribution of magma types in the ignimbrite record and corresponding tephra record (Harmon et al., Part 1), we establish the sequence of eruption for the four different mappable ignimbrites. The ignimbrites to the east of the caldera (Rangitaiki ± Te Whaiti) erupted before the Whakamaru ignimbrite (sensu stricto) to the west of the caldera. The youngest Whakamaru ignimbrite eruptions likely deposited to the northwest of the caldera contemporaneously with the Manunui ignimbrite to the west of the caldera. We calculate pre-eruptive storage temperatures (via zircon saturation geothermometry) and pressures (via rhyolite-MELTS geobarometry) using the glass compositions of the pumice clasts. We determine pressures of extraction from magma mush (via rhyolite-MELTS geobarometry) using matching whole-rock compositions. Melt-dominated magmas were stored at shallow depths (~50-150 MPa) prior to eruption. Types B and C extraction pressures are well constrained to 155-355 MPa. For types A and D, extraction pressures depend on the modeled oxygen fugacity (fO2), exhibiting a narrower range given a specific fO2 (overall range 170-360 MPa). Our results suggest there are at least two different

magma subsystems that fed the Whakamaru eruptions – one subsystem sourced the type A and type D magmas, while the other sourced the type B and type C magmas. Both subsystems show gaps between storage and extraction pressures, suggesting separation between melt-dominated magma bodies and the magma mush bodies from which they were extracted. Combination of petrological data from the ignimbrites and associated tephras suggest a complex system that included laterally juxtaposed melt-dominated magmas as well as laterally juxtaposed magma mushes that spanned much of the shallow crust, but with regions in which magma appeared in low concentration or was entirely absent. Ignimbrite deposition across the landscape follows patterns revealed by the chronology observed in the tephra sequence.

KEY WORDS

Whakamaru group ignimbrites; Whakamaru ignimbrite; Rangitaiki ignimbrite; Manunui ignimbrite; Te Whaiti ignimbrite; Taupō Volcanic Zone; magma storage; geobarometry; magma extraction; glass geochemistry; pumice

INTRODUCTION

Large, explosive volcanic eruptions demonstrate that the crust must create and accommodate large volumes of melt-dominated magma prior to eruption. Melt-dominated magma bodies that source these extreme volcanic events are thought to be ephemeral features (Charlier *et al.*, 2007; Wilson and Charlier, 2009; Gualda *et al.*, 2012b; Cooper and Kent, 2014; Stelten *et al.*, 2014; Pamukçu *et al.*, 2015a; Gualda and Sutton, 2016; Cooper *et al.*, 2017; Shamloo and Till, 2019). Substantial advances have been made to understand the pre-eruptive conditions of the melt-dominated magma bodies that feed such eruptions (Cashman & Giordano, 2014), including crystallization timescales (Simon and Reid, 2005; Charlier *et al.*, 2008; Druitt *et al.*, 2012; Allan *et al.*, 2013; Barboni and Schoene, 2014; Chamberlain *et al.*, 2014; Cooper and Kent, 2014; Pamukçu *et al.*, 2015a; Gualda and Sutton, 2016; Fabbro *et al.*, 2017; Reid and Vazquez, 2017; Shamloo and Till, 2019; Chakraborty and Dohmen, 2022); storage pressures (Blundy and Cashman, 2008; Hansteen and Klügel, 2008; Putirka, 2008; Ridolfi *et al.*, 2010; Gualda and Ghiorso, 2013a; Bégué *et al.*, 2014a; Bachmann and Huber, 2016; Gualda *et al.*, 2018; Pitcher *et al.*, 2021; Pelullo *et al.*, 2022); volatile content (Moore *et al.*, 1998; Papale *et al.*, 2006; Ghiorso and Gualda, 2015; Waters and Lange, 2015; Iacovino *et al.*, 2021; Wieser *et al.*, 2022); and oxygen fugacity (f_{O2}) conditions (Kelley and Cottrell, 2009; Pitcher *et al.*, 2021; Ghiorso *et al.*, 2023). These eruptions have a variety of possible pre-eruptive storage configurations as they can erupt from one magma body, as in the ‘mush’ model (Hildreth, 1979; Bachmann and Bergantz, 2004, 2008; Hildreth and Wilson, 2007; Deering *et al.*, 2011; Pamukçu *et al.*, 2013; Chamberlain *et al.*, 2015; Foley *et al.*, 2020) or from multiple melt-dominated magma bodies (Bégué, Deering, *et al.*, 2014; Cashman & Giordano, 2014; Cooper *et al.*, 2012;

Gravley *et al.*, 2007; Gualda & Ghiorso, 2013b; Pearce *et al.*, 2020; Swallow *et al.*, 2018). This precludes a one-model-fits-all approach to understanding melt-dominated magmatic bodies.

It is increasingly recognized that magmatism is a crustal-scale phenomenon (Annen *et al.*, 2015; Cashman *et al.*, 2017; Karakas *et al.*, 2017; Weinberg *et al.*, 2021; Hilley *et al.*, 2022), such that there is increasing interest in constraining the depths from which melt-dominated magmas are extracted from magma mush (Gualda *et al.*, 2019; Blundy, 2022). In contrast to the melt-dominated magma bodies, the bodies of magma mush from which melt-dominated magmas are extracted can be much longer lived and they can be much more widespread in their vertical distribution in the crust (Annen *et al.*, 2015; Reid and Vazquez, 2017; Gualda *et al.*, 2019; Sparks *et al.*, 2019; Blundy, 2022; Giordano and Caricchi, 2022).

Studying magma mushes is limited by the fact that they are only rarely erupted; and even when they are entrained in eruptions, they have often been modified by reheating and remobilization (Bindeman and Valley, 2003; Deering *et al.*, 2011; Pamukçu *et al.*, 2013; Wolff, 2017; Foley *et al.*, 2020). Evidence for mush is present in granitic plutons (Harper *et al.*, 2004; Tavazzani *et al.*, 2020; Wiebe *et al.*, 2021; Wallrich *et al.*, 2023), but the holocrystalline nature of granites hampers understanding the mechanical and chemical evolution of mushes and the specific eruptions they eventually produce. Extraction pressures (Gualda *et al.*, 2019) allow us to use erupted volcanic rocks to derive important information on the location of magma mushes in the crust (Pamukçu *et al.*, 2021; Pitcher *et al.*, 2021; Smithies *et al.*, 2023). Understanding how the crust can produce melt-dominated magma from the magma mush is paramount in elucidating the dynamics of large magmatic systems.

The Taupō Volcanic Zone (TVZ) Whakamaru group eruptions expelled >2000 km^3 of melt-dominated, rhyolitic magma from a large magmatic system (see also Harmon *et al.*, Part 1).

The eruptions kicked off a period of high volcanic activity (i.e., an ignimbrite flare-up, Gravley *et al.*, 2016), which led to the eruption of – in addition to the Whakamaru group itself – six caldera-forming eruptions over the ensuing ~100 ka (see also Gualda *et al.*, 2018; Smithies *et al.*, 2023). The Whakamaru group ignimbrites are known to have erupted pumice of multiple compositions (Brown *et al.*, 1998; Harmon *et al.*, Part 1) indicating the presence of multiple magma types in the magmatic system. Here, we investigate the pre-eruptive magmatic conditions (temperature, pressure, and composition) for melt-dominated magma bodies, as well as the extraction conditions for magma mush bodies from the Whakamaru group eruptions.

We use matrix-glass and whole-rock compositions to identify compositional groups, as well as to determine storage and extraction conditions. Further, we correlate our results for pumice from the ignimbrites presented here with data from co-erupted pyroclastic fall deposits (Harmon *et al.*, Part 1) to constrain the timing of eruption of the various ignimbrite packages that make up the Whakamaru group ignimbrites. The ultimate goal is to understand what the crust looks like prior to volcanic eruptions, which can help us understand how the crust can produce such active magmatic and volcanic systems.

The terminology we use here follows Smithies *et al.* (2023) and Harmon *et al.* (Part 1), demonstrated schematically in Figure 1. A ***magma body*** is a parcel of magma that is in contact with rocks or other magmas, with clear boundaries. We define melt-dominated magma bodies and magma mush bodies. A ***melt-dominated magma body*** is composed of crystal-poor magma that typically has a suspension of crystals (and possibly bubbles). It can be erupted imminently. Melt-dominated magma is extracted from the ***magma mush body***. A ***magma mush body*** is composed of crystal-rich magma that contains a framework of touching crystals with interstitial melt (± bubbles). The magma mush is unlikely to be readily erupted. A ***magma type*** is a

compositionally and texturally homogeneous group of magmas where a given magma type may be characteristic of a magma body, or it may be present in multiple magma bodies. The ***magma system*** includes all magma bodies through time. We follow Gualda *et al.* (2019) and distinguish ***contiguous magma bodies***, in which melt-dominated magma is in direct contact with magma mush, as typically invoked in the 'mush' model (Bachmann and Bergantz, 2004, 2008; Hildreth, 2004), and ***non-contiguous magma bodies***, in which melt-dominated magma is detached from the magma mush body from which it was extracted.

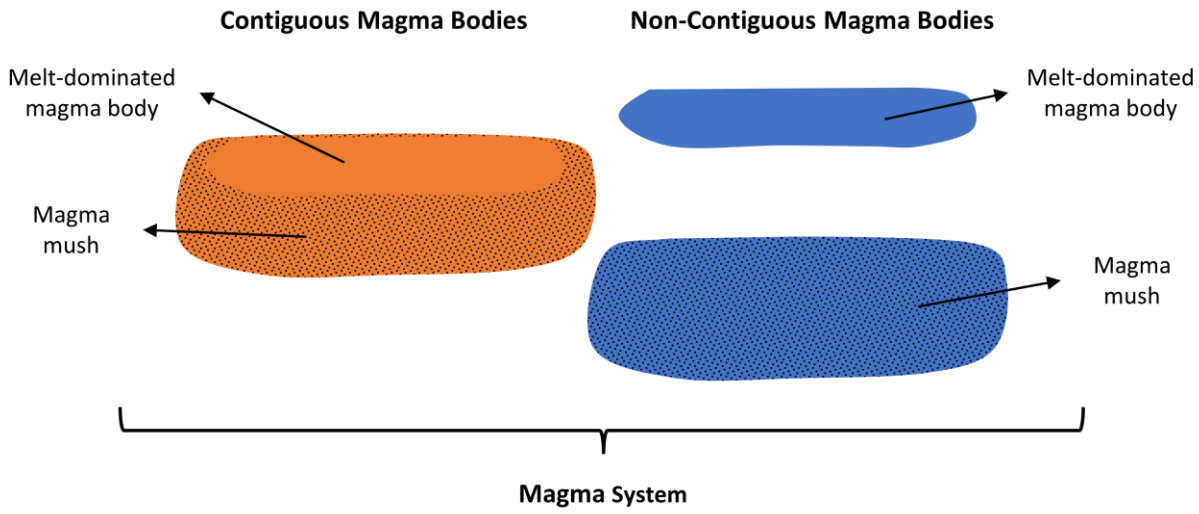

Figure 1 Schematic of a magma system and its constituents. A magma body is a parcel of magma that is in contact with rocks or other magmas, with clear boundaries. We subdivide magma bodies into melt-dominated magma bodies and magma mush bodies. A magma type is compositionally and texturally homogeneous group of magmas; in this diagram, there are two magma types, represented by the blue and orange colors. The relationship between melt-dominated and mush bodies can be either contiguous or non-contiguous, depending on if the melt-dominated magma body is in contact with the magma mush from which it was extracted (contiguous), or if the melt-dominated magma has migrated to a shallower storage zone (non-contiguous). There can be multiple

geochemically related magma bodies existing at a single time in the crust. The magma system includes all magma bodies through the lifetime of the system.

GEOLOGIC BACKGROUND

The Taupō Volcanic Zone (TVZ) is a rifted arc (Wilson *et al.*, 1995) situated in the central North Island of Aotearoa New Zealand (Figure 2); it is one of the most active silicic volcanic regions in the world (Houghton *et al.*, 1995; Wilson *et al.*, 1995). There have been three documented pulses of intense volcanic activity (Houghton *et al.*, 1995), known as ignimbrite flare-ups, over the ~1.9 Ma history of silicic volcanism in the TVZ (Eastwood *et al.*, 2013; Chambefort *et al.*, 2014). The most intense ignimbrite flare-up from ~350 to ~240 ka, included seven large ignimbrite-forming eruptions (Houghton *et al.*, 1995; Gravley *et al.*, 2007, 2016; Wilson *et al.*, 2009) and began with the largest eruptions of the young TVZ history – the Whakamaru eruptions (Wilson *et al.*, 1986; Leonard *et al.*, 2010; Downs *et al.*, 2014; Gravley *et al.*, 2016). Prior to the Whakamaru group eruptions, there was a period of relative quiescence in the TVZ lasting ~200 ka (Deering *et al.*, 2010), wherein there were no documented caldera-forming eruptions between the Utu and Whakamaru group eruptions. The Whakamaru magma system explosively erupted >2000 km^3 DRE (Wilson *et al.*, 1986; Houghton *et al.*, 1995; Matthews *et al.*, 2012c; Downs *et al.*, 2014) of relatively crystal-rich magma (~15-40 wt.% crystals) (Martin, 1961, 1965; Houghton *et al.*, 1995; Brown *et al.*, 1998). These eruptions are unique within the TVZ as they sometimes contain sanidine (Brown *et al.*, 1998; Downs *et al.*, 2014; Harmon *et al.*, Part 1) and are characterized by a “cold, wet, oxidizing” signature (Deering *et al.*, 2010). The subsequent eruptions of this ignimbrite flare-up period show a stark transition in composition and style (Wilson *et al.*, 2009; Gravley *et al.*, 2016), as they are smaller by an order of magnitude (50-150 km^3 DRE), typically crystal poor (<10 wt% crystals), and exhibit a

158 "hotter, dryer, less oxidizing" magmatic signature (Ewart, 1967a, 1967b; Wilson *et al.*, 2009;
159 Deering *et al.*, 2010; Leonard *et al.*, 2010).

160 The Whakamaru magmas erupted from relatively shallow storage depths of ~50-150 MPa
161 (Brown *et al.*, 1998; Matthews, 2011; Gualda *et al.*, 2018; Harmon *et al.*, Part 1), typical of the
162 TVZ (Bégué *et al.*, 2014b; Gualda *et al.*, 2018). The compositional change following the
163 Whakamaru group eruptions is also marked by a change in the pressure that the melt-dominated
164 magma bodies feeding the caldera-forming eruptions were stored – deeper storage conditions
165 were observed shortly after Whakamaru eruptions, followed by a progressive shallowing through
166 the flare-up (Gualda *et al.*, 2018; Smithies *et al.*, 2023). In the early stages of the post-
167 Whakamaru eruptions of the flare-up, extraction pressures are relatively deep, with the range of
168 extraction pressures increasing to include shallower levels over time (Gualda *et al.*, 2019;
169 Smithies *et al.*, 2023).

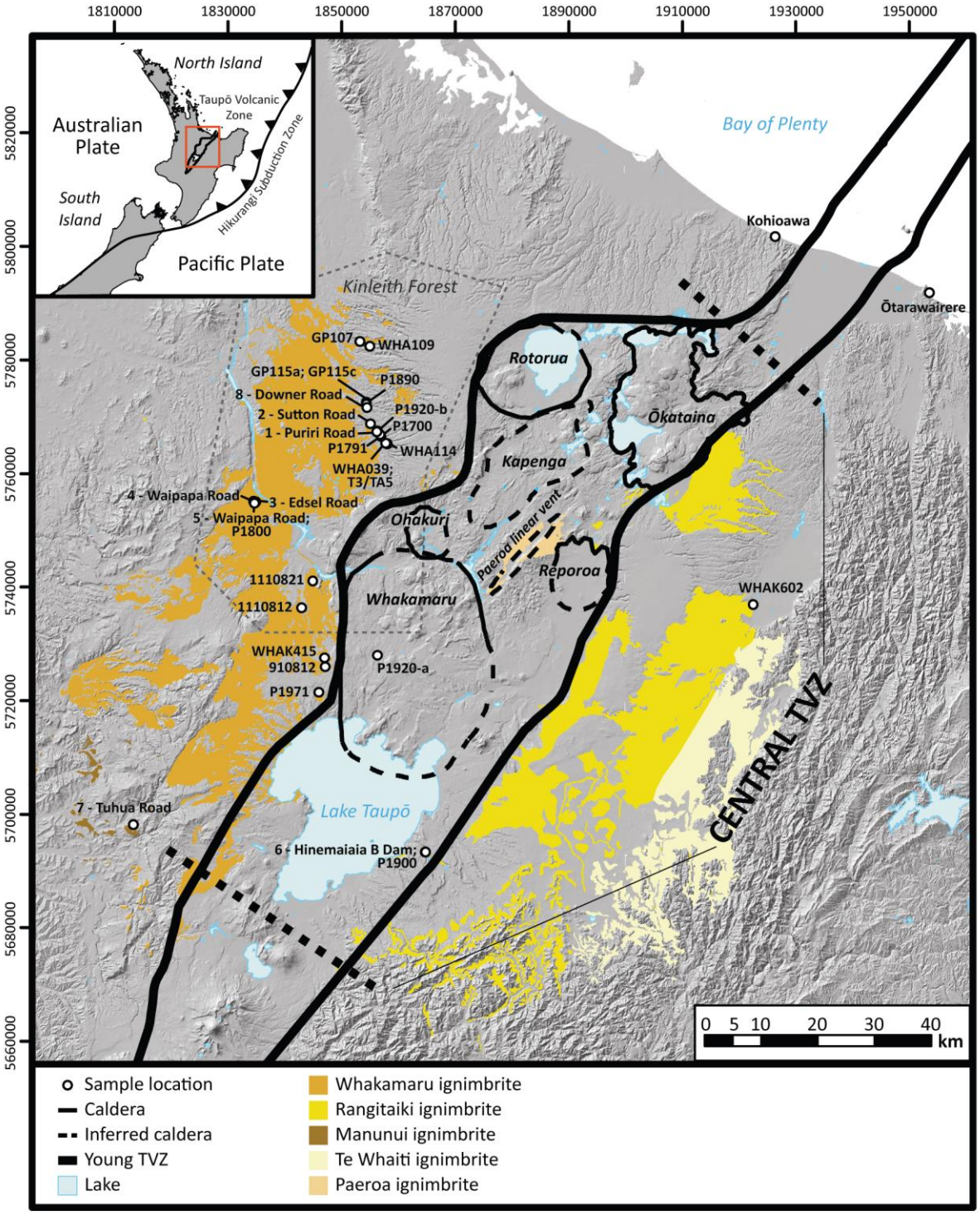

Figure 2 Map of the Taupō Volcanic Zone (TVZ), New Zealand, showing the outline of the young TVZ and major calderas of the ignimbrite flare-up (~350-240 ka). The Whakamaru group eruptions originated from the Whakamaru caldera. These eruptions

include the Whakamaru and Manunui ignimbrites distributed to the west of the caldera and the Rangitaiki and Te Whaiti ignimbrites distributed to the east of the caldera at 349 ± 4 ka (Downs *et al.*, 2014). The younger Paeroa Subgroup erupted from the Paeroa linear vent at 339 ± 5 ka (Downs *et al.*, 2014). Sample locations are marked, with most samples collected in the Kinleith Forest area. Samples from this study are labeled with names starting with "GP", "WHA", and "WHAK". These samples are supplemented with samples from Brown *et al.* (1998) and Matthews (2011). The two sample locations at the coast, labeled Kohioawa and Ōtarawairere, are the locations of the pyroclastic fall deposits (tephras) of Harmon *et al.* (Part 1). Calderas are mapped after Leonard *et al.* (2010), outline of the young TVZ after Wilson *et al.* (1995), and the Whakamaru group ignimbrites are shown after Leonard *et al.* (2010), Brown *et al.* (1998), and Downs *et al.* (2014). Coordinate system is in meters in the New Zealand Transverse Mercator 2000 projected on the New Zealand Geodetic Datum 2000. The map inset shows the location of the TVZ within the North Island of New Zealand.

Previous work on the Whakamaru Group Ignimbrites

The Whakamaru group eruptions have long been recognized as a major volcanic event in the central TVZ (Briggs, 1976a, 1976b; Ewart & Healy, 1966; Grindley, 1960; Martin, 1965; Wilson *et al.*, 1984, 1986, 2009). Previous field, petrographic, and compositional work reveal that >2000 km^3 DRE erupted (Wilson *et al.*, 1986; Matthews *et al.*, 2012c; Downs *et al.*, 2014). The deposits are mapped as multiple ignimbrites (Grindley, 1960; Ewart and Healy, 1966; Briggs, 1976a, 1976b; Wilson *et al.*, 1986; Brown *et al.*, 1998), but the number of eruptive phases – one (Brown *et al.*, 1998; Downs *et al.*, 2014) or multiple (Grindley, 1960; Martin, 1961; Wilson *et al.*, 1986; Houghton *et al.*, 1995) – is disputed. There are five wide-spread, mappable

ignimbrite units that make up the Whakamaru Group ignimbrites: the Whakamaru (*sensu stricto*), Manunui, Rangitaiki, and Te Whaiti, and the younger Paeroa Subgroup, which is interpreted to have erupted from a nearby source (Downs *et al.*, 2014) (Figure 2). However, we focus on the four main ignimbrites of the Whakamaru group eruptions. The three ignimbrites that were dated (the Whakamaru, Rangitaiki, and Te Whaiti ignimbrites) have the Ar-Ar age of 349 ± 4 ka (Downs *et al.*, 2014) with the younger Paeroa Subgroup having the Ar-Ar age of 339 ± 5 ka (Downs *et al.*, 2014). The Manunui and Whakamaru ignimbrites are distributed to the west of the caldera, and the Te Whaiti and Rangitaiki ignimbrites are distributed to the east of the caldera (Grindley, 1960; Wilson *et al.*, 1986; Leonard *et al.*, 2010). The four ignimbrites are described in Table 1 based on previous work (predominantly by Brown *et al.* (1998) and references therein), including degree of welding, crystal contents, and compositional types of pumice found in each ignimbrite.

The volcanology and petrology of the Whakamaru group are complex, and the ignimbrites are notoriously difficult to place in stratigraphic order, as overlap in the field is insufficient to definitively determine the relative ages of the various ignimbrite deposits (Wilson *et al.*, 1986; Brown *et al.*, 1998). Importantly, the radiometric ages of the three Whakamaru group mappable units that have been dated (Whakamaru, Rangitaiki, and Te Whaiti) show that they erupted within error of each other (Downs *et al.*, 2014). Earlier work suggests that the deposits represent multiple eruptive episodes (Grindley, 1960; Martin, 1961; Wilson *et al.*, 1986; Houghton *et al.*, 1995), while later work (Brown *et al.*, 1998; Downs *et al.*, 2014) suggests that they could be erupted as one main eruption phase. Wilson *et al.* (1986) propose that the Manunui and Te Whaiti ignimbrites erupted earlier and could be correlative, while the Whakamaru and Rangitaiki ignimbrites erupted later and could be correlative. Multiple pulses have been

established in both the Rangitaiki and Te Whaiti ignimbrites (Briggs, 1976b), further demonstrating the complex eruptive history of the ignimbrites.

Brown *et al.* (1998) define four compositional types of rhyolite pumice – types A, B, C, and D – with a minor amount of mingled basalt. The four types (Briggs, 1976a; Brown *et al.*, 1998) are categorized by mineralogy and whole-rock chemical composition (Table 2). In the Whakamaru ignimbrite, all four pumice types are found, while in the other ignimbrites, a more restricted pumice population is observed (Table 1) (Brown *et al.*, 1998; Matthews, 2011). We attempt to constrain the eruption timing of the different magma types and their relationships to the different ignimbrites.

The sources and maturation of the Whakamaru system have been described from the zircon ages (Brown and Fletcher, 1999; Matthews, 2011) and plagioclase compositions (Saunders *et al.*, 2010). Zircon ages from type A and D pumice clasts show a long-lived and complex history of magma evolution (Brown & Fletcher, 1999; Matthews, 2011). There is debate about the timing of the initiation of the Whakamaru system, as Brown & Fletcher (1999) indicate a 250 ka history, while Matthews (2011) more extensive data set has a peak of zircon ages that imply a ~50-100 ka history for most of the magma system. Compositional and textural evidence from plagioclase crystals indicate multiple sources for the magma system and that a complex history of mingling, mixing, and homogenization ultimately yielded the Whakamaru magmas (Saunders *et al.*, 2010). The compositions (i.e., anorthite (An) content, as well as Ba, Sr, La concentrations) of plagioclase crystals suggest that both crustal melts of the underlying metasedimentary basement rock, which is corroborated by Sr ad Pb isotopes from pumice clasts (Brown *et al.*, 1998) and mantle-derived melts are the ultimate sources of magma for the Whakamaru magma system (Saunders *et al.*, 2010).

Ti-in-quartz diffusion timescales allow us to estimate the maximum crystallization time of the melt-dominated rhyolite magma body (Gualda *et al.*, 2012b; Pamukçu *et al.*, 2015a; Gualda and Sutton, 2016). For types A and D pumice clasts from the Whakamaru and Rangitaiki ignimbrites, timescales of 1-10 ka suggest that the melt-dominated magmas that fed the Whakamaru eruptions existed for no longer than 10 ka and possibly as little as 1 ka (Matthews *et al.*, 2012a; Gualda *et al.*, 2018). Quartz rims indicate that the final pulse of crystallization was <300 years prior to eruption (Saunders *et al.*, 2010). Evidence from quartz crystals agrees with the general observation that large melt-dominated magma bodies are ephemeral crustal features (Gualda *et al.*, 2012b; Cooper and Kent, 2014; Pamukçu *et al.*, 2015a; Gualda and Sutton, 2016; Matthews *et al.*, 2012a; Charlier et al., 2008; Allan *et al.*, 2017; Shamloo and Till, 2019). To summarize, evidence from both zircon (Brown and Fletcher, 1999; Matthews, 2011) and plagioclase crystals (Saunders *et al.*, 2010) indicates that the Whakamaru magma system was established over a longer time, and evidence from quartz crystals (Saunders *et al.*, 2010; Matthews *et al.*, 2012b; Gualda *et al.*, 2018) shows short storage time of melt-dominated magma bodies prior to eruption.

Nomenclature

The Whakamaru magma system refers to all associated melt-dominated magma bodies and magma mush bodies. We use Whakamaru group ignimbrites when referring to all the material erupted as pyroclastic flows. We specify the single Whakamaru ignimbrite when it is necessary to distinguish it from the other (i.e., Rangitaiki, Te Whaiti, Manunui) ignimbrites.

METHODS

Sampling

We sampled from a total of eight outcrops throughout the Whakamaru group ignimbrites, detailed in Figure 2 and Supplemental Data. We chose the largest and freshest pumice clasts available at the outcrops. Due to the predominantly welded nature of the ignimbrites (Briggs, 1976a; Brown *et al.*, 1998), finding unwelded pumice with pristine glass is challenging. We tried to sample from a variety of locations and ignimbrites, although the quality of exposures and the existence of unwelded pumice led us to sample predominantly from the Whakamaru ignimbrite. Thirty-five samples are from the Whakamaru ignimbrite from five different outcrops within the Kinleith forest (the northernmost samples on the west side of the TVZ), and an additional location to the north of Lake Taupō and one to the east of Lake Taupō (Figure 2). We collected four samples from the Rangitaiki ignimbrite from one location. We found no fresh, glassy pumice in either the Manunui or the highly welded Te Whaiti ignimbrite deposits, so we did not analyze any Manunui or Te Whaiti pumice. In the future, analyzing glass from the Manunui and Te Whaiti bulk ignimbrites could allow us to further investigate these ignimbrites. We supplement our data with whole rock data from Brown *et al.* (1998) and Matthews (2011), which includes pumice clasts from the Whakamaru, Rangitaiki, and Manunui ignimbrites.

Sample preparation

Each pumice clast was brushed lightly in water to remove bulk tephra and then dried in an oven at ~50 °C for ~24 hours. After cleaning, each pumice clast was stored individually to minimize contamination.

Pumice geochemistry

Glass geochemistry

Major- and trace-element glass compositions were obtained using the same methods as detailed in Harmon *et al.* (Part 1) on all 39 pumice clasts. The methods are also summarized below. For every pumice clast, we picked a small (<1 cm^3) piece of the interior of the pumice clast, to make sure no bulk ignimbrite was incorporated during analyses. We mounted the pumice pieces in epoxy, before polishing and carbon coating for analysis.

The glass major-element compositions were obtained at Vanderbilt University using an Oxford X-max 50-mm2 Energy Dispersive Spectrometer (EDS) attached to a Tescan Vega 3 LM Variable Pressure Scanning Electron Microscope (SEM). Most glass analyses were obtained using 15 kV accelerating voltage (with several obtained with an accelerating voltage of 18-20 kV to achieve a higher output count rate) and a specimen current of ~4 nA at a working distance of 15 mm. Data collection and quantification was performed using the program AZtec from Oxford Instruments, using process time 4 and employing pulse pile-up corrections. For each sample, we analyzed ~15 spots of the largest, most pristine sections of glass, far from crystals. For each pumice clast, analyses were excluded if 1) a mineral (usually feldspar or a Fe-Ti oxide) was encountered; 2) the SiO_2 was >82 wt.%; 3) the composition lay outside 1.5 times the interquartile range (IQR) for that individual lapillus. This IQR test was performed once, and not iteratively, to identify and remove outliers that fall outside the natural variability of the glass (see Harmon *et al.*, Part 1). After removing outliers and problematic analyses, we identify potentially different populations within a single pumice clast, however all glass compositions seem consistent on the pumice-clast scale for this study. We then calculate the mean and standard deviation for each pumice clast. We use the standard deviation for each clast as the best measure of uncertainty,

because it is invariably larger than the calculated analytical uncertainty. The USGS-Rhyolite Glass Mountain (RGM-1) standard was measured at the beginning of each SEM session as a secondary standard. Results from the USGS RGM-1 standard are provided in the supplementary data. As demonstrated by Pamukçu *et al.* (2015b, 2021), glass data obtained with EDS-SEM is of quality similar to or better than data obtained by the electron microprobe analyzer (see also (Reed and Ware, 1973; Ritchie *et al.*, 2012).

The trace-element glass compositions were obtained via Laser Ablation Inductively Coupled Plasma Mass Spectrometry (LA-ICPMS) at Vanderbilt University. The system is a Photon Machines Excite 193 nm excimer laser attached to a Thermo iCAP Q quadrupole ICPMS system. For each analysis, a 50 μm × 50 μm square laser spot size was ablated for 25 s at a pulse frequency of 10 Hz. NIST 610 was used as the primary standard and NIST 612 and RGM-1 were used as secondary standards. The isotope ^{28}Si was used as an internal standard, using the average SiO_2 contents determined for each sample by EDS-SEM analysis prior to trace-element analysis. Concentrations were processed through the data reduction program Glitter (Griffin *et al.*, 2008; van Achterbergh *et al.*, 2001).

We analyzed ~15 spots per pumice clast for trace-element compositions using LA-ICPMS, where the spot locations were not the same as those analyzed for major-element compositions via EDS-SEM. Similarly to the treatment we used for major elements, trace-element analyses were discarded if: 1) a mineral (usually feldspar or a Fe-Ti oxide) was encountered or 2) if an analysis had at least 5 elements below the detection limit. Individual analytes were discarded if they failed the same IQR method as the major element data. Trace-element data from individual pumice clasts were not considered further if <3 spots provided adequate compositional analyses for a given pumice clast.

We then computed averages and standard deviations for each pumice clast or population, and we use the standard deviations as our best measure of uncertainty given that they are larger than the calculated analytical errors.

Whole-rock geochemistry

A subset of pumice clasts (16) were analyzed via x-ray fluorescence (XRF) spectrometry to determine whole-rock compositions. Pumice clasts chosen for whole-rock XRF analysis were the largest clasts, and we chose clasts that exhibit different pumice types based on the glass compositions of the pumice clasts. Analysis was completed by Hamilton Analytical Lab (https://www.hamilton.edu/academics/analytical-lab), using a Thermo Scientific ARL Perform'X sequential XRF spectrometer. Routine operating conditions of the spectrometer are 45 kV accelerating voltage at 45 mA. A total of 72 reference materials are used for calibration. Drift is monitored with in-house standards that are run every 3-4 weeks. One duplicate unknown was prepared and analyzed to check for sample homogeneity and reproducibility of data. Loss on Ignition (LOI)-eliminated influence coefficients are used for matrix correction. Calibration reference materials are chiefly those issued by the USGS and GSJ, but also include reference materials from CRPG, GIT-IWG, NIST, BAS, Mintek, and other sources. The revised USGS, GSJ, and CRPG RM values provided in Jochum *et al.* (2016) were employed and weighted more heavily than the values from other reference materials.

Geobarometry

Recent work focusing on storage pressures of magma bodies demonstrates that it is possible to use measured glass compositions with a known (or inferred) mineral assemblage to constrain storage pressures of pyroclastic rocks (Gualda *et al.*, 2012a; Bégué *et al.*, 2014b; Gualda and Ghiorso, 2014; Pamukçu *et al.*, 2015b; Harmon *et al.*, 2018; Harmon *et al.*, Part 1).

We use glass compositions from pumice clasts to calculate rhyolite-MELTS pre-eruptive storage pressures (Bégué *et al.*, 2014b; Gualda and Ghiorso, 2014; Pamukçu *et al.*, 2015b; Harmon *et al.*, 2018; Smithies *et al.*, 2023). We also use whole-rock compositions to calculate the pressure at which the melt-dominated magma was extracted from the mush (hereafter termed "extraction pressure", see Gualda *et al.* (2019) and Smithies *et al.* (2023) and the "launching point" of Blundy (2022). We model the storage and extraction pressures using the methods outlined in previous papers. We set MnO and P_2O_5 to 0 wt.%, and – for glass compositions – we set MgO to 0.05 wt.% if the measured value is below the analytical detection limit (and is reported as 0 wt%). For both glass and whole-rock compositions, we model from 500-25 MPa in 25 MPa steps, from 1100-700 °C in 1 °C steps, with 10 wt.% H_2O to impose fluid saturation in all calculations. Gualda and Ghiorso (2014) and Ghiorso and Gualda (2015) show that H_2O does not have a substantial effect on pressure calculations and any H_2O in excess of saturation does not impact the calculations. For the glass compositions, we fixed the f_{O2} to the NNO buffer (Δ NNO = 0) in rhyolite-MELTS calculations; for the whole-rock compositions, we explored a range of f_{O2} parameters from f_{O2} equal to the NNO buffer (Δ NNO = 0) to 1.5 log units above NNO in half log unit steps (Δ NNO = +0.5, +1, +1.5), which encompasses the reasonable ranges of f_{O2} for the system (Deering *et al.*, 2010; Matthews, 2011). We consider the that the melts were stored in equilibrium with two possible phenocryst mineral assemblages: 1) quartz + feldspar (qtz-1feld) and 2) quartz + plagioclase + sanidine (qtz-2feld) (Gualda & Ghiorso, 2014). For the extraction calculations, we consider that the magmas were extracted from two possible mush mineral assemblages: 1) quartz + feldspar (qtz-1feld); and 2) feldspar + orthopyroxene (feld-opx) (Bégué *et al.*, 2014a; Harmon *et al.*, 2018; Gualda *et al.*, 2019; Pitcher *et al.*, 2021; Smithies *et al.*, 2023).

Zircon geothermometry

Zircon-saturation temperatures are calculated using the average major-element glass compositions and average Zr concentrations in the glass of the pumice clasts using the formulations of Watson & Harrison (1983) and Boehnke *et al.* (2013) (Gualda and Ghiorso, 2013b; Foley *et al.*, 2020; Pitcher *et al.*, 2021; Gualda *et al.*, 2022). If zircon is saturated, the calculated temperature represents the temperature of zircon-melt equilibrium (likely a pre-eruptive storage temperature); if zircon is undersaturated, the calculations return minimum temperatures. From previous work on zircon chemistry and age dating, zircon has been studied extensively in types A and D pumice from the Whakamaru and Rangitaiki ignimbrites (Brown & Fletcher, 1999; Matthews, 2011). This previous work (Brown, 1994; Brown and Fletcher, 1999; Matthews, 2011) and pumice whole-rock and glass chemistry presented here suggest zircon is ubiquitously saturated in the Whakamaru group ignimbrites.

RESULTS

Pumice geochemistry

Brown *et al.* (1998) define four predominant compositional pumice types – types A, B, C, and D, which are distinguished primarily based on whole-rock Rb and Sr values (Table 2). Our whole-rock data contain pumice from all four magma types, confirmed by comparing our whole-rock data to Brown *et al.* (1998) and Matthews (2011) (Tables 3 and 4 and Figure 3).

In addition to the whole-rock compositions, we can distinguish types A, B, and C by their matrix glass compositions (Table 4 and Figure 4), following the classification based on glass from pyroclastic fall deposits (i.e., tephras) correlative with the Whakamaru group ignimbrites (Harmon *et al.*, Part 1). We can distinguish type A from types B and C by CaO and TiO_2 major-element glass compositions, and we can distinguish types A, B, and C (especially type B from

type C) by the Ba and Sr trace-element glass compositions. Using matching whole-rock and glass pairs for several pumice clasts presented in this study, we confirm that the A, B, and C groups identified by Harmon *et al.* (Part 1) using tephra glass compositions match the original A, B, and C types identified by Brown *et al.* (1998) (Figure 5). Type D pumice clasts are distinguishable from other pumice types in whole-rock composition but are not readily distinguished by the glass compositions (as glass compositions are very similar to those of type A). Since we have whole-rock data for only one type D pumice clast, we cannot definitively distinguish type D glass – this means that we cannot identify type D from type A pumice clasts for which we do not also have whole-rock compositions. However, type D is considered a more minor component of the ignimbrites (Brown *et al.*, 1998).

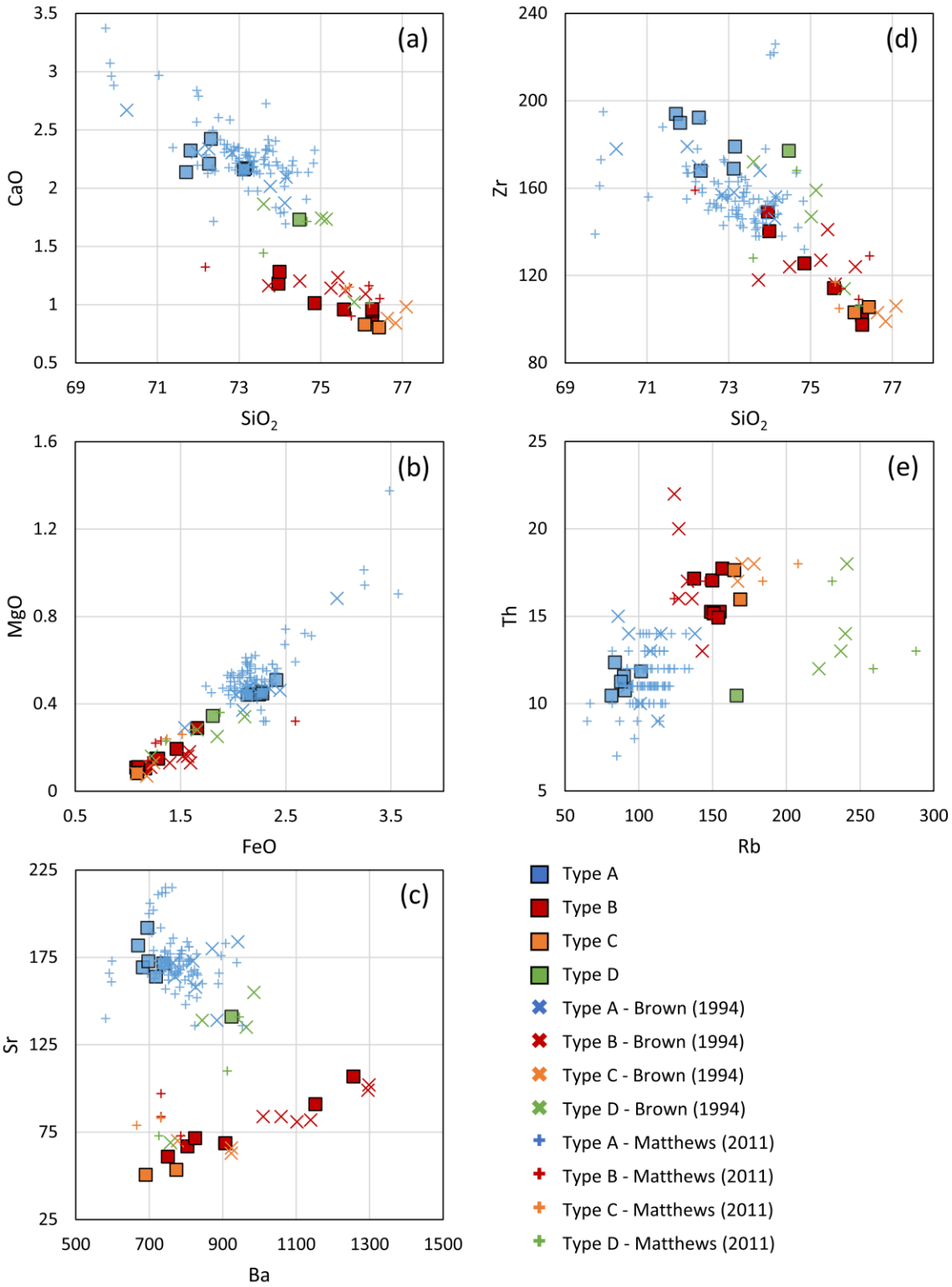

409

410 **Figure 3** Whole-rock compositions of pumice clasts from the Whakamaru group

411 ignimbrites in a) CaO vs. SiO_2; b) MgO vs. FeO; c) Sr vs. Ba; d) Zr vs. SiO_2; and e) Th

vs. Rb space. Major elements (SiO_2, CaO, FeO, MgO) are reported as weight percent (wt. %) of the oxide normalized anhydrous; trace elements (Zr, Th, Rb, Sr, Ba) are reported in parts per million (ppm). Data presented here are represented by filled-in squares. Literature data from Brown (1994) are represented by x's. Literature data from Matthews (2011) are represented by +'s. The four compositional groups (types A, B, C, D) are established from Brown *et al.* (1998) and are represented by colors, where type A is blue, type B is red, type C is orange, and type D is green. Pumice clasts of compositional type A and type D have been demonstrated to contain plagioclase but not sanidine. Pumice clasts of compositional type B and type C have been demonstrated to contain plagioclase and sanidine. Quartz is ubiquitous in all compositional pumice types (Brown *et al.*, 1998).

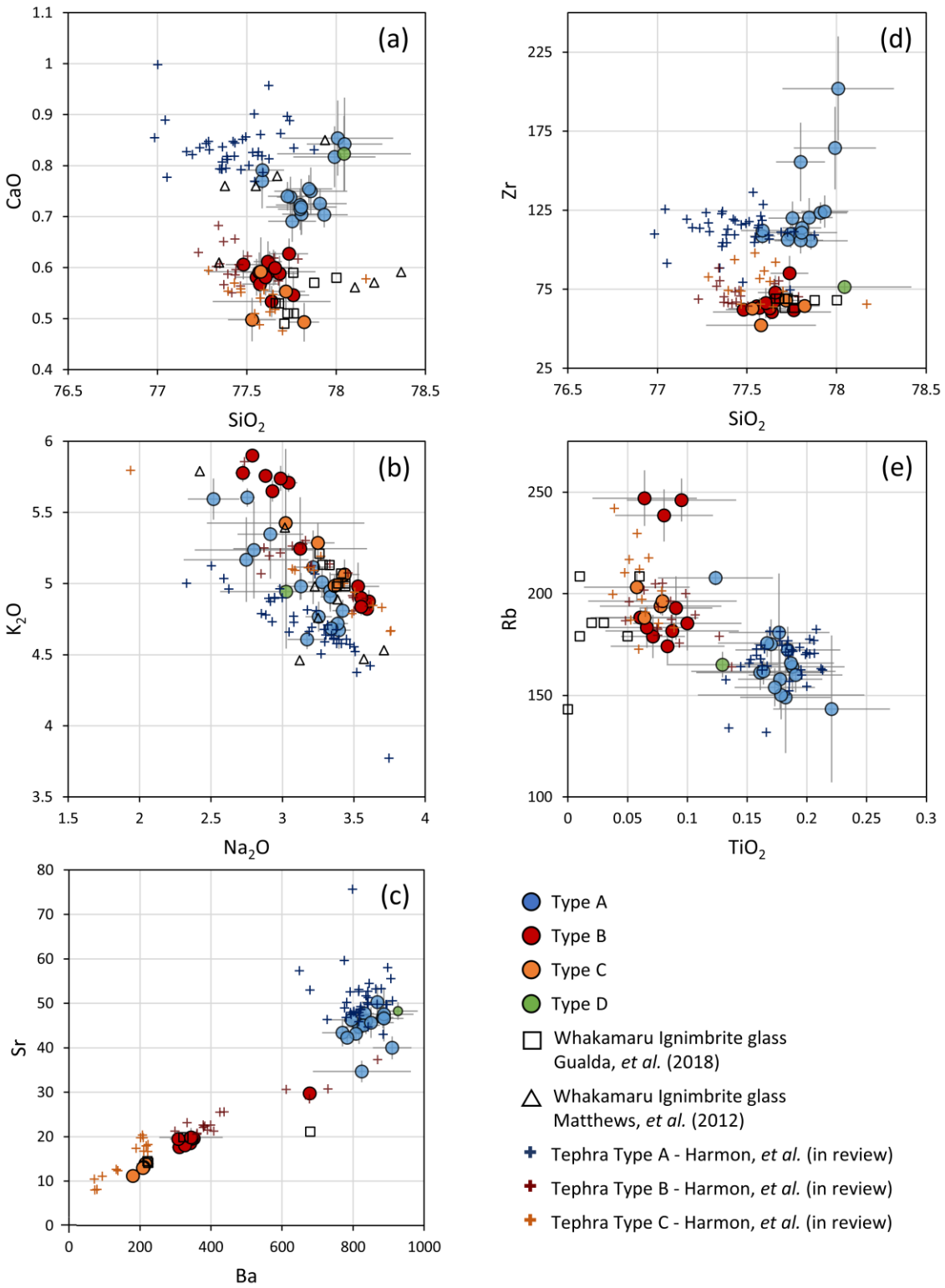

Figure 4 Major- and trace-element glass compositions from pumice clasts of the Whakamaru group ignimbrites in a) CaO vs. SiO_2; b) MgO vs. FeO; c) Sr vs. Ba; d) Zr

426 vs. SiO_2; and e) Th vs. Rb space. Major elements (SiO_2, CaO, K_2O Na_2O, TiO_2) are
427 reported as wt.% of the oxide normalized anhydrous; trace elements (Zr, Rb, Sr, Ba) are
428 reported in ppm. The four types (A, B, C, D) are established from whole-rock
429 composition data from pumice clasts that have matching glass and whole-rock data.
430 Literature data from the tephra deposits correlated to the Whakamaru eruptions from
431 Harmon *et al.* (Part 1) are represented by +'s, literature ignimbrite glass data from the
432 Whakamaru ignimbrite from Gualda *et al.* (2018) are represented by small squares and
433 from Matthews *et al.* (2012) are represented by small triangles.

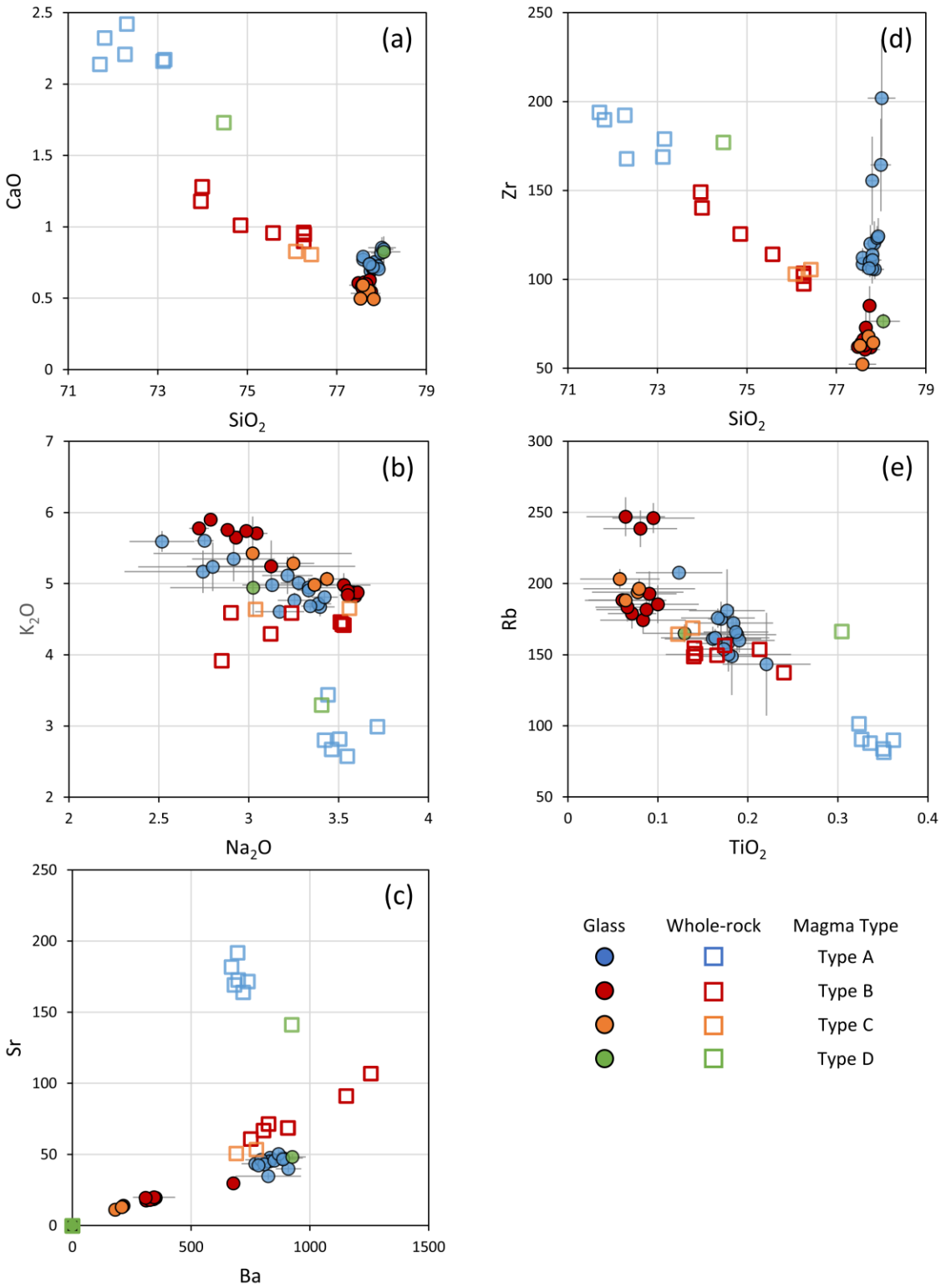

Figure 5 Glass and whole-rock compositional data from Whakamaru group ignimbrite pumice clasts. Major elements (SiO_2, CaO, K_2O Na_2O, TiO_2) are reported as wt.% of the

oxide; trace elements (Zr, Rb, Sr, Ba) are reported in ppm. Whole-rock data are represented by squares; glass data are represented by filled circles. Data are subdivided into types A, B, C, and D based primarily on whole-rock compositions. The pumice clasts that only had compositional data for glass were subdivided based on their chemical similarity to pumice clasts with both whole-rock and glass compositions. The glass compositions converging to high SiO_2 values indicates that all magma types have high-silica rhyolite melt compositions.

Whole-rock geochemistry

The sixteen pumice whole-rock compositions range from 71.7-76.4 wt.% SiO_2, 0.8-2.4 wt.% CaO, 81-169 ppm Rb, and 51-192 ppm Sr. Using the Brown *et al.* (1998) classification discussed above, there are 6 type A pumice clasts, 7 type B pumice clasts, 2 type C pumice clasts, and 1 type D pumice clast (16 total). Their compositional signatures are highlighted in Figures 3 and 5 and Table 3.

Glass geochemistry

We analyzed matrix glass of 41 pumice clasts (Table 4), with two showing altered glass compositions with SiO_2 >82 wt.% that are not further discussed. For 15 of the pumice clasts that have both whole-rock and glass data (all except WHAK415-A2), we use the whole-rock classification from Brown *et al.* (1998) in addition to the tephra classification for glass from Harmon *et al.* (Part 1) to determine the pumice type. For the pumice clasts that do not have matching whole-rock data, we rely on the tephra glass classification of Harmon *et al.* (Part 1) (Figures 4 and 5). There are sixteen type A samples (one of which does not have trace-element compositions due to culling the analyses, detailed in the methods), fourteen type B samples (four of which do not have trace-element compositions), four type C samples, and one type D sample.

The four pumice clasts collected from the Rangitaiki ignimbrite do not fall into any of the categories defined by Brown *et al.* (1998), and do not have similar compositions to each other. Their anomalously high Rb content and low Sr content indicate that they likely do not represent pristine glass compositions. We refer to these pumice clasts as "unclassified". They are mapped in Figures 2 and 6 but are neither plotted nor discussed further. We supplement our data with whole-rock compositions from Matthews (2011) and Brown *et al.* (1998).

Distribution of pumice types

The Whakamaru ignimbrite (*sensu stricto*) has pumice from all four compositional types (types A, B, C, D). The Manunui ignimbrite has four samples: 1 type A, 1 type C, and 2 type D samples (Brown *et al.*, 1998; Matthews, 2011). The Rangitaiki ignimbrite contains exclusively type A from the pumice analyzed in previous studies (Brown, 1994; Brown *et al.*, 1998; Matthews, 2011) (Figure 6). We did not analyze pumice clasts from Te Whaiti pumice due to the welded nature of the deposits, and there is limited information available in the literature (Brown, 1994; Brown *et al.*, 1998; Matthews, 2011).

The various outcrops of the Whakamaru ignimbrite show possible variation in the proportion of different pumice types (Figure 6). In the northwest portion of the deposits (i.e., Kinleith forest, outlined in Figures 2 and 6), there is a concentration of outcrops that have type C pumice in addition to types A and B pumice clasts, with many outcrops exhibiting more than one type of pumice. The majority of the western and southern Whakamaru deposits are dominated by type A and type B pumice, with smaller abundance of type D pumice (Figure 6 and Table 4).

There are several locations (4 from the Whakamaru ignimbrite, 1 from the Rangitaiki ignimbrite, and 1 from the Manunui ignimbrite) whose locations from Matthews (2011) appear to be documented incorrectly, as they lie substantially outside of the mapped distribution of the

ignimbrites. We include the data in Figure 6; however, the data are plotted in boxes on the corresponding sides of the caldera near the corresponding ignimbrite deposits. From these data, all pumice clasts from the Whakamaru ignimbrite and Rangitaiki ignimbrite are reported to be type A, while the two samples from the Manunui ignimbrite are reported to be type A and type D. This indicates that a portion of the Whakamaru ignimbrite contains exclusively type A, and that the Rangitaiki ignimbrite exhibits exclusively type A pumice thus far, although the precise locations of these sample sites are unknown.

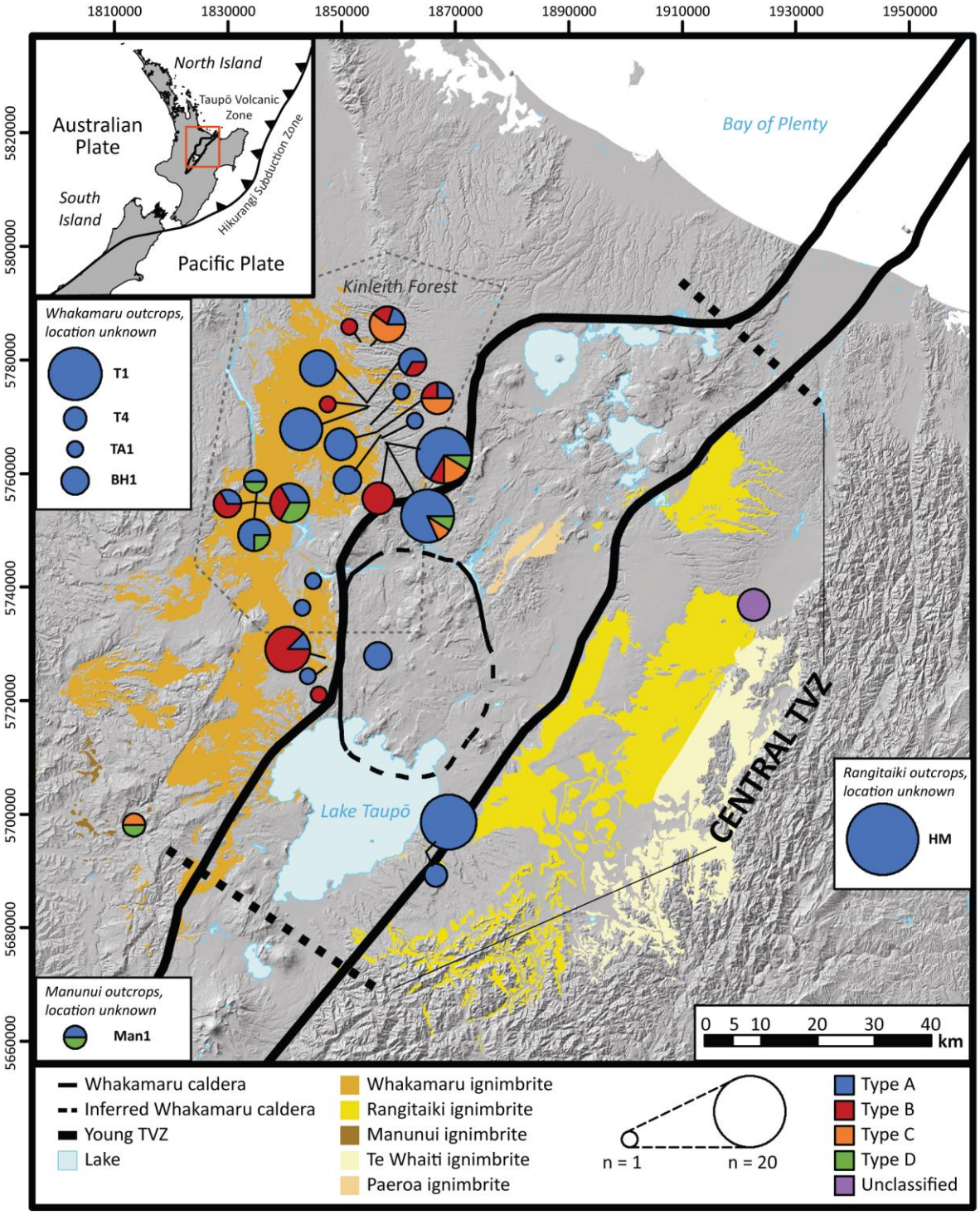

Figure 6 Map of the TVZ, showing the distribution of pumice types at the different sampling locations. The colors of the pie-charts represent the different pumice types (types A, B, C, D), and the size of the pie chart represents how many pumice clasts are

analyzed at each location. The Kinleith forest area has the highest sampling density, to the north of the caldera within the Whakamaru ignimbrite. Five sample locations from Matthews *et al.* (2011) are unknown. The samples from those locations are shown in white boxes near to the ignimbrite from which they were collected.

Geobarometry

Storage assemblages and pressures

Overall, storage pressures calculated from glass compositions are shallow, ranging from 45-140 MPa (1.7-5.4 km depth, assuming a crustal density of $2.7*10^3$ kg/m^3). We report the results of each pumice type below, with results summarized in Figure 7 (circles correspond to qtz-1feld storage pressures and triangles correspond to qtz-2feld storage pressures calculated using glass compositions) and Table 4. We report individual pressure calculations to the nearest MPa (e.g., 122 MPa), and we report ranges of pressures to the nearest 5 MPa (e.g., 100-135 MPa) Uncertainties of storage pressure calculations by Pitcher *et al.* (2021) determine a 1-sigma standard deviation of 24 MPa for qtz-2feld pressures and 38 MPa for qtz-1feld pressures. Smithies *et al.* (2023) performed a Montecarlo error analyses on the sample WHA114-A (type B) using an f_{O2} of ΔQFM = +1.5, which exhibited a qtz-2feld pressure of 133 MPa and 1-sigma standard deviation of 13 MPa with several qtz-1feld results showing <22 MPa 1-sigma standard deviation. In all figures that contain geobarometry results, we plot the more conservative uncertainties of Pitcher *et al.* (2021).

Of the sixteen type A glass compositions, twelve return storage pressures. Only one composition (WHAK415-A5) returns a qtz-2feld pressure, while the other eleven compositions return qtz-1feld pressures. Of the fourteen type B glass compositions, nine return qtz-2feld pressures and an additional three return qtz-1feld storage pressures; the shallowest pressure (75

517 MPa) is one of the compositions that yields a qtz-1feld storage pressure. Of the four type C glass
518 compositions, three return qtz-2feld pressures; the shallowest pressure (75 MPa) corresponds to a
519 qtz-1feld storage pressure. The one type D sample returns a qtz-1feld storage pressure
520 assemblage.

521 As has been documented in previous studies (Bégué *et al.*, 2014b; Gualda *et al.*, 2018;
522 Harmon *et al.*, Part 1), there are a minority of compositions that produce coincident or sub-
523 parallel quartz and feldspar saturation surfaces at pressures ≤ 100 MPa. For these compositions,
524 we follow the method detailed by Bégué *et al.* (2014) and report the highest pressure that has a
525 residual temperature ≤ 5 °C. There are five compositions that are affected – WHA039C (100
526 MPa; type A), WHA039H (100 MPa; type A), WHA039F (75 MPa; type B), WHA109B (75
527 MPa; type C), and WHAK415-A6 (75MPa; type D). We note that these pressures are maxima
528 (Bégué *et al.*, 2014b).

529 We calculate average storage pressures of 92 ± 18 MPa (1-sigma) (3.5 ± 0.7 km) for type
530 A, 118 ± 23 MPa (4.5 ± 0.9 km) for type B, 94 ± 19 MPa (3.6 ± 0.7 km) for type C, and 75 MPa
531 (2.8 km) for the single type D glass composition.

532 Previous studies (Ewart, 1965; Martin, 1965; Briggs, 1976a; Brown *et al.*, 1998)
533 demonstrate that pumice types A and D do not have sanidine, while types B and C do have
534 sanidine. Therefore, types A and D should not produce qtz-2feld storage pressures, and the qtz-
535 1feld assemblage is expected for the storage pressures. Because sanidine is present, rhyolite-
536 MELTS should return qtz-2feld storage pressures for types B and C, which is indeed reflected by
537 the majority of the storage pressures calculated via rhyolite-MELTS. This pattern is consistent
538 with what was observed in the correlative fall-derived tephras studied by Harmon *et al.* (Part 1).
539 The several samples that do not produce pressures likely reflect the sensitivity of rhyolite-

MELTS to the input compositions – in other words, we infer that glass compositions that do not yield pressures are altered or affected by analytical artifacts (Bégué *et al.*, 2014b; Gualda and Ghiorso, 2014; Pamukçu *et al.*, 2015b). The success yield in type A compositions is lower than in other types, which could suggest alteration, perhaps due to Na-K exchange (see Figure 4) (Pamukçu *et al.*, 2015b).

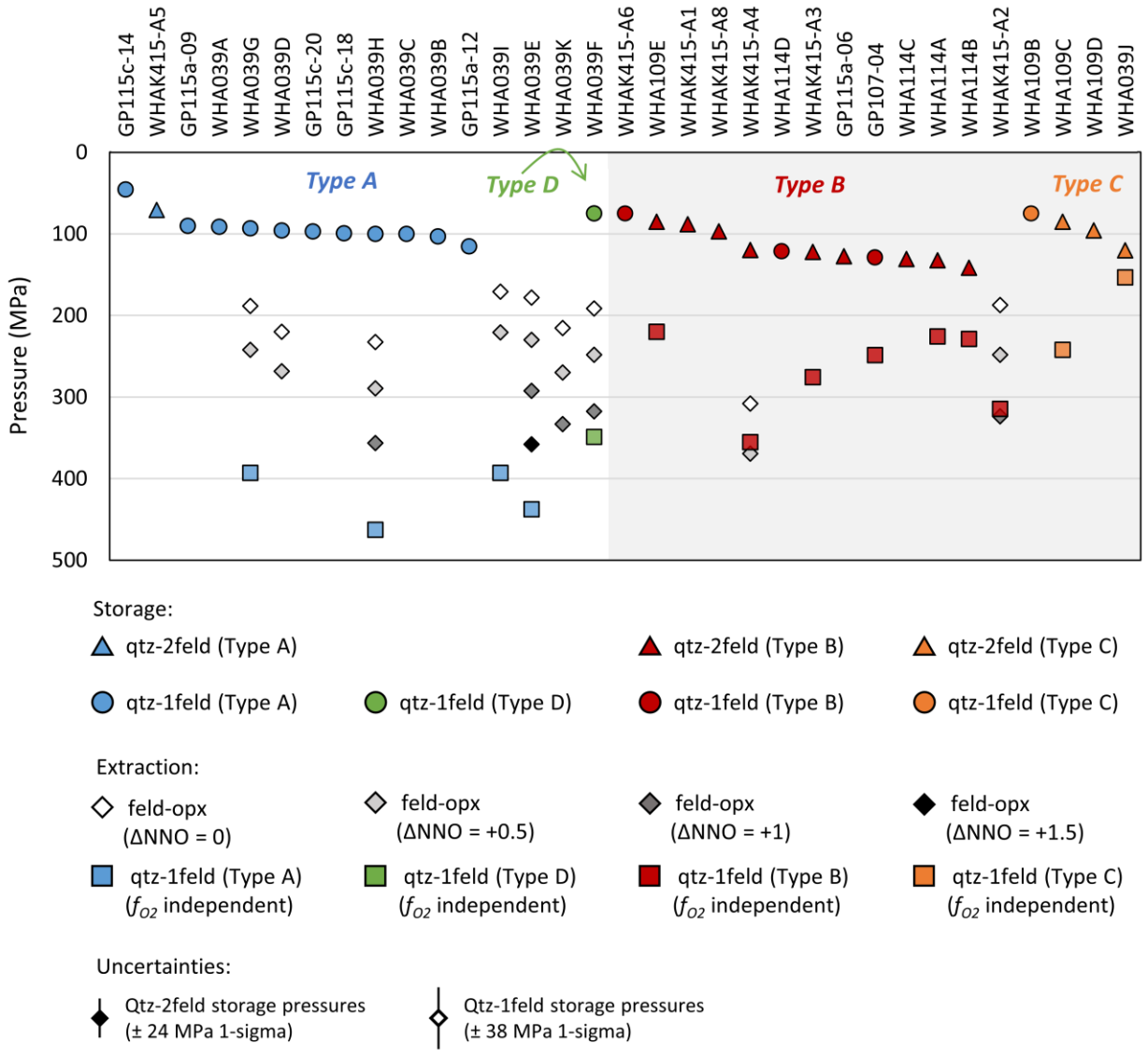

Figure 7 Magma storage and extraction pressures from rhyolite-MELTS calculations, represented by the rank-order of the storage pressures. The storage pressures utilize the

glass compositions as an input to the rhyolite-MELTS modeling, and the magma extraction pressures utilize the whole-rock compositions as the input to the rhyolite-MELTS modeling. Storage pressures are represented by circles (qtz-1feld storage assemblage) and triangles (qtz-2feld storage assemblage) and show the final storage pressures of the melt-dominated magma bodies prior to eruptions. The extraction pressures represented by diamonds (feld-opx extraction assemblage) and squares (qtz-1feld extraction assemblage) show from what depth the melt was extracted from the magma mush bodies. The extraction pressures are dependent on f_{O2}. The diamonds represent the feld-opx extraction pressures at increasing f_{O2} (Δ NNO 0 = white, Δ NNO +0.5 = light gray, Δ NNO +1 = medium gray, and Δ NNO + 1.5 = black). The colored squares represent the qtz-1feld extraction pressures, which are not dependent on f_{O2}. The qtz-1feld extraction pressures represent the deepest possible extraction pressures in this case. Magma types A and D have an extraction assemblage of feld-opx at lower f_{O2} and feld-opx±qtz at higher f_{O2} (ΔNNO +1.5).

Extraction assemblages and pressures

We consider two possible extraction assemblages – quartz + feldspar (qtz-1feld) or feldspar + orthopyroxene (feld-opx) – both of which are considered potential assemblages for the TVZ mush bodies that source the melt-dominated magma bodies (Gualda *et al.*, 2019; Smithies *et al.*, 2023). In the rifted central TVZ, there is a sharp density transition at 16 km depth, which is inferred to be the Moho (Stern *et al.*, 2006) or, alternatively, heavily intruded lower crust (Harrison & White, 2006). Therefore, the maximum crustal extraction pressures would be ~425 MPa, assuming a crustal density of $2.7*10^3$ kg/m^3. All of the extraction pressures obtained here are <400 MPa, but the calculated extraction pressures depend on the extraction assemblage

considered and oxygen fugacity (f_{O2}). Extraction pressures and assemblages are reported in Figure 7 (squares correspond to qtz-1feld pressures and diamonds correspond to feld-opx pressures calculated using whole-rock compositions) and Table 3.

All seven of the whole-rock analyses for types A and D produce extraction pressures. The feld-opx extraction pressures range between 170-235 MPa (6.5-8.8 km) for f_{O2} equal to the NNO buffer (Δ NNO = 0). The extraction pressures increase with increasing f_{O2}. However, fewer valid extraction pressures are obtained with increasing f_{O2}. Both Δ NNO = 0 and Δ NNO = +0.5 produce seven extraction pressures; Δ NNO = +1 produces four extraction pressures; Δ NNO = +1.5 produces one extraction pressure. We calculate the following range of extraction pressures: 170-235 MPa (6.5-8.8 km) for Δ NNO = 0, 220-290 MPa (8.3-10.9 km) for Δ NNO = +0.5, 290-355 MPa (11.0-13.5 km) for Δ NNO = +1, and 360 MPa (13.5 km) for Δ NNO +1.5. At f_{O2} fixed at Δ NNO = +1 to Δ NNO = +1.5, two compositions produce quartz + feldspar + orthopyroxene (qtz-1feld-opx) pressures. For the other compositions, the quartz saturation curve is close to the feld-opx intersection, indicating that there could be quartz present at the source if the f_{O2} is high (e.g., Δ NNO = +1 to Δ NNO = +1.5), which agrees with some of the existing f_{O2} estimates (Brown *et al.*, 1998; Deering *et al.*, 2010). However, Matthews (2011) estimates f_{O2} to be between Δ NNO = 0 and Δ NNO = +0.5, indicating that types A and D would have been extracted from a feld-opx bearing mush (that does not contain quartz) at shallower pressures.

All nine whole-rock compositions for types B and C produce extraction pressures. All compositions produce qtz-1feld extraction pressures, with a range of 155-355 MPa (5.8-13.4 km), with most pressures 220-310 MPa (8.3-11.7 km). There are only two compositions that yield feld-opx extraction pressures – WHAK415-A4 has a feld-opx extraction pressure of 310 MPa (11.7 km) at an f_{O2} of Δ NNO = 0, and WHAK415-A2 has a feld-opx extraction pressures

of 190 MPa (7.2 km) at an f_{O2} of Δ NNO = 0 and 250 MPa (9.4 km) for an f_{O2} of Δ NNO = +0.5. None of the other compositions yield viable feld-opx pressures – in all cases, the orthopyroxene saturation curve is below the quartz or feldspar saturation curves. Since the qtz-1feld extraction pressures are shallower than the feld-opx pressures, and the quartz saturation curve is above the feld-opx intersection, we can disregard the feld-opx pressures (i.e., it is not possible for feldspar and orthopyroxene to be stable without quartz also being stable, which means the qtz-1feld is the only assemblage consistent with the modeling results for that given composition, irrespective of f_{O2}). The type C sample WHA039J sample has the shallowest extraction pressure (153 MPa; 5.8 km), which is just slightly deeper than the type C storage pressures.

Zircon-saturation temperatures

Zircon is likely saturated in all magma types (Brown, 1994), which is supported by our whole-rock and glass pairs, showing lower Zr concentrations in glass when compared to whole-rock, indicating that some Zr is fractionated into zircon (Figures 5 and 8) (Foley *et al.*, 2020). Using the average glass compositions, we calculate zircon saturation temperatures of 791 ± 28 °C (1-sigma) for type A, 750 ± 17 °C for type B, 741 ± 9 °C for type C, and 752 °C for the type D sample using the Watson and Harrison (1983) calibration. Using the Boehnke *et al.* (2013) calibration, the average zircon saturation temperatures are 759 ± 33 °C (1-sigma) for type A, 711 ± 19 °C for type B, 701 ± 11 °C for type C, and 712 °C for type D. All individual calculations are reported in Table 4. Generally, we see that types A samples are relatively hotter, while types B, C, and D are relatively cooler.

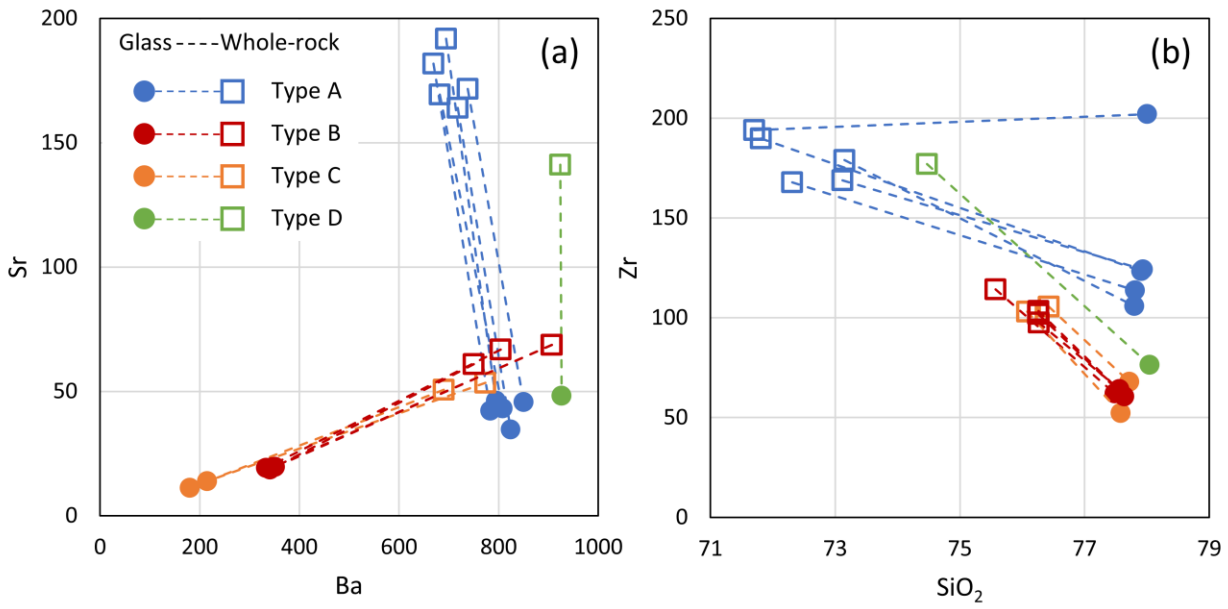

Figure 8 Compositional data for individual pumice clasts that have both whole-rock and glass compositions in a) Sr vs Ba and b) Zr vs SiO_2 space. SiO_2 is reported as wt.% of the oxide; trace elements (Sr, Ba, Zr) are reported in ppm. The whole-rock compositions are represented by open squares, and the glass compositions are represented by filled circles where whole-rock and glass compositions of each individual clast are connected by a dashed line. The different pumice compositional types (A, B, C, D) are represented by different colors. In general, type A and type D follow similar trends, and type B and type C follow similar trends. In a) all types have higher Sr in the whole-rock than in the glass, with type B and type C having <50 ppm Sr in the glass. For Ba, type A and type D have a lower concentration in the whole-rock in comparison to the glass; in contrast, type B and type C have a higher Ba concentration in the whole-rock in comparison to the glass. In b) all types have a higher concentration of Zr in the whole-rock rock in comparison to the glass compositions, with the exception of one type A composition. For SiO_2, all compositions show lower SiO_2 whole-rock compositions in comparison to the glass compositions, indicating a convergence to high-silica rhyolite glass in all pumice clasts.

This suggests that all magmas were saturated in plagioclase, quartz, and zircon, as evidenced by the lower concentrations of Sr, Zr, and SiO_2 in glass relative to whole rock. However, only types B and C were also saturated in sanidine, as evidenced by the lower concentration of Ba in these glasses relative to whole rock.

DISCUSSION

Pre-eruptive storage conditions of the melt-dominated magma bodies

Four distinct types of magma sourced the Whakamaru eruptions (Brown *et al.*, 1998). Our samples can first be categorized into two overarching geochemical groups based on whole-rock and glass compositions, as well as mineralogy. Samples of pumice types A and D have higher Sr and CaO in whole-rock compositions (Figures 2 and 8) and higher Sr, Ba, and Zr in glass compositions in comparison to types B and C (Figures 3 and 8). Pumice clasts of types B and C form a second group, having lower Sr and Zr in whole-rock compositions (Figures 2 and 8), generally more fractionated glass compositions with lower Ba and Sr and slightly higher Rb (Figure 4). These characteristics are consistent with the presence of sanidine in types B and C, and the absence of sanidine in types A and D (Brown *et al.*, 1998; Harmon *et al.*, Part 1).

The paired whole-rock and glass compositions from the individual pumice clasts provide evidence for the saturation (or undersaturation) of various mineral phases in the different magma types. The presence of zircon is ubiquitous in all four magma types (type A, B, C, and D), as evidenced by the higher concentration of Zr in the whole rock in comparison to the glass of the same pumice clasts (Figure 8). Zr is a major constituent of the mineral zircon, so a lower concentration in the glass implies that a portion of the Zr is contained within zircon crystals in the pumice clast. A similar argument can be made for the presence of the feldspars – plagioclase and sanidine. All four magma types have a lower concentration of Sr in the glass when compared

to the whole-rock compositions, indicating that all four magma types are saturated in plagioclase. Due to the preferential uptake of Ba in sanidine, lower Ba contents in the glass relative to whole-rock demonstrate sanidine saturation in types B and C, while types A and D show higher Ba in glass than whole-rock, consistent with absence of sanidine (see Figure 8). This matches the well-established mineralogy from Brown *et al.* (1998), and references therein, and confirms the inferences from Harmon *et al.* (Part 1) based on rhyolite-MELTS storage pressure calculations. The presence of sanidine is unusual within the TVZ, with the Whakamaru group ignimbrites being one of the few units to contain sanidine.

Similar to what was found using the correlative tephras (Harmon *et al.*, Part 1), results for rhyolite-MELTS storage pressures presented here support the distribution of sanidine in the different pumice types: most storage pressures for types A and D are not sanidine-bearing (producing qtz-1feld pressures, Figures 7 and 9), while most storage pressures for types B and C are sanidine-bearing (producing qtz-2feld pressures, Figures 7 and 9). This suggests that – at least in the case of the Whakamaru group magmas – rhyolite-MELTS can be effectively used to infer the felsic mineralogy in equilibrium with each magma type, which is particularly useful when direct observation is not possible (see Harmon *et al.*, Part 1).

Zircon-saturation geothermometry helps to further parse these groups (Table 4). The geothermometry suggests that type A was stored at a hotter temperature (~40-60 °C hotter) than types B, C, and D. Together, the geothermometry and geobarometry results suggest at least 3 distinct melt-dominated magma bodies (A, B+C, D). Despite overlapping storage assemblages and pressures, the distinct trace-element glass compositions of types B and C (Figures 4 and 7) suggests they were likely two different melt-dominated magma bodies, indicating that the four magma types represent at least four magma bodies. Since there is little overlap in either whole-

rock or glass compositions among the different magma types, the melt-dominated magma bodies likely did not mix prior to eruption (see also Harmon *et al.*, Part 1).

Considering our rhyolite-MELTS geobarometry results in more detail also provides some insights into the arrangement of these magma bodies in the crust. The rhyolite-MELTS storage pressures are all similarly shallow (Figures 7 and 9), indicating that each magma type occupies a narrow range of storage depths in the upper crust. This is consistent with the predominantly shallow storage pressures of caldera-forming rhyolite magmas in the central TVZ (Bégué *et al.*, 2014a). Interestingly, there is no difference in the pressure distribution between the three main magma types (A, B, and C; Figure 9), consistent with the findings of Harmon *et al.* (Part 1) that the Whakamaru group eruptions were fed by laterally juxtaposed melt-dominated magma bodies – and in contrast with the vertically stratified single magma chamber model advocated by Brown *et al.* (1998). This adds to the growing evidence that supereruptions can be fed by a patchwork of laterally juxtaposed melt-dominated magma bodies (Cooper *et al.*, 2012, 2017; Bégué *et al.*, 2014a; Pearce *et al.*, 2020; Gualda *et al.*, 2022).

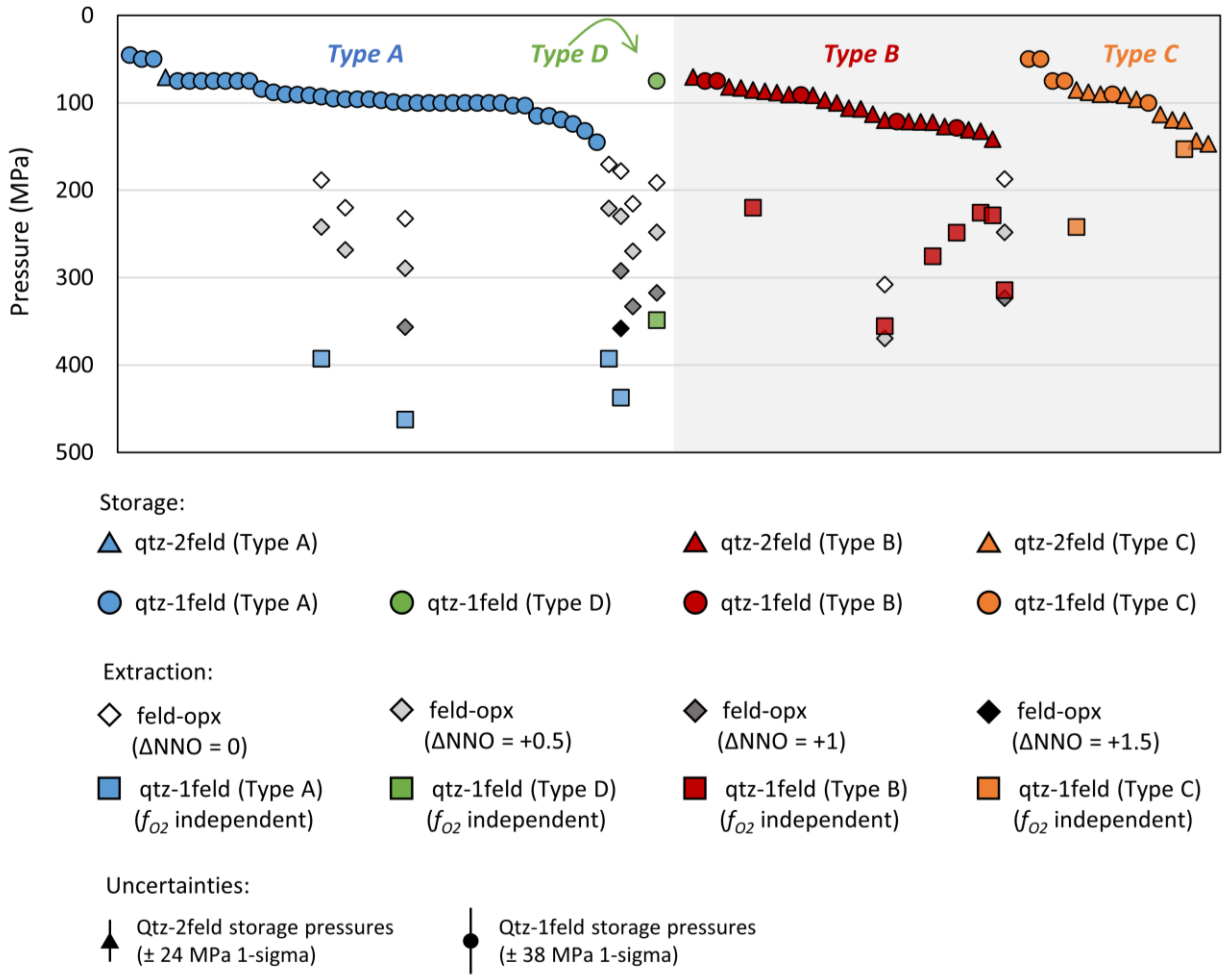

Figure 9 Magma storage and extraction pressures from rhyolite-MELTS calculations, represented by the rank-order of the storage pressures from this work and from Harmon *et al.* (Part 1). See Figure 7 for an explanation of the symbology and modeling details. The combination of the data from the tephra and from the ignimbrites shows consistent storage pressures for the Whakamaru group eruptions.

Extraction conditions and the depths of magma mush bodies

Extraction pressures provide insight into the organization of magma mush bodies in the crust as a function of depth, as well as – when combined with storage pressures – their positions relative to the melt-dominated magma bodies extracted from them (Figure 1) (Gualda *et al.*,

2019; Smithies *et al.*, 2023). Previous work in the TVZ shows that both contiguous and non-contiguous storage has occurred in the region (Gualda *et al.*, 2019).

Extraction pressures for types B and C magmas are much better constrained than for types A and D, given that types B and C extraction pressures are only consistent with a quartz + feldspar (qtz-1feld) assemblage, which is independent of f_{O2}. Type B magma extraction occurred at depths in the range of 220-360 MPa (~8-13 km), and type C extraction occurred at depths in the range of 150-240 MPa (~5.5-9.0 km). This suggests contiguous extraction for type C, and non-contiguous extraction for type B magmas (Figure 10).

Types A and D magmas are distinct from types B and C in their extraction characteristics. For type A and D compositions, extraction pressures for a plagioclase + orthopyroxene (feld-opx) assemblage are typically lower (indicating shallower extraction) than for a qtz-1feld assemblage, suggesting equilibration with an assemblage consisting of plagioclase and orthopyroxene. Due to the sensitivity of orthopyroxene stability on f_{O2} conditions, extraction pressures increase with increasing f_{O2}. For the range of f_{O2} that we tested for (NNO to NNO+1.5 log units), resulting extraction pressures vary from 170 MPa to 460 MPa for types A and D magmas. We are left with two competing hypotheses:

1. If f_{O2} is low (ΔNNO < 1), all magma types are extracted from a shallower depth (~150-360 MPa) with two different assemblages (types A and D extracted from a mush with a feld-opx assemblage; types B and C extracted from a mush with a qtz-1feld assemblage)
2. If f_{O2} is high (ΔNNO > 1), the magmas are extracted from different depths with different assemblages (types A and D extracted from a mush up to ~290-460 MPa with feld-opx±qtz and types B and C still extracted from ~150-360 MPa from a mush with a qtz-1feld assemblage)

A low f_{O2} (ΔNNO < 1) is consistent with the estimates by Matthews (2011). This would imply that the different magma types are extracted from similar crustal levels with different assemblages, which could signal that there is a tectonic or structural control of where in the crust the mush bodies develop. If the f_{O2} is higher (ΔNNO > 1), which agrees with the estimates by Brown *et al.* (1998) and Deering *et al.* (2010), then the source of type A and D magmas likely included feldspar + orthopyroxene ± quartz at deep pressures, implying that the base of the TVZ crust is saturated in quartz for this system. In either scenario, the extraction of types A and D occurs over a narrow range.

Both SiO_2 concentrations in the whole-rock compositions and zircon saturation temperatures can help constrain which extraction scenario is more likely. The relatively wide range of SiO_2 whole-rock compositions for type A and type D indicate that quartz is likely not present (undersaturated) at the source, in contrast with the case of the Taupō Ignimbrite, see Pamukçu *et al.* (2021), in which the SiO_2 concentration in the whole-rock compositions are tightly constrained within ~1 wt% SiO_2, indicating that quartz is present (saturated) at the source. If quartz is not present at the source, then the f_{O2} values of Matthews (2011) and the lower end of the f_{O2} values from Deering *et al.* (2011) are more likely. This provides evidence for all magma types being extracted from a similar, more shallow level (Figure 10). It is difficult to ascertain if the magma mush bodies were saturated in zircon or not; nonetheless, the higher Zr contents of whole-rock type A pumice suggests that extraction temperatures could have been higher for type A when compared to types B and C magmas.

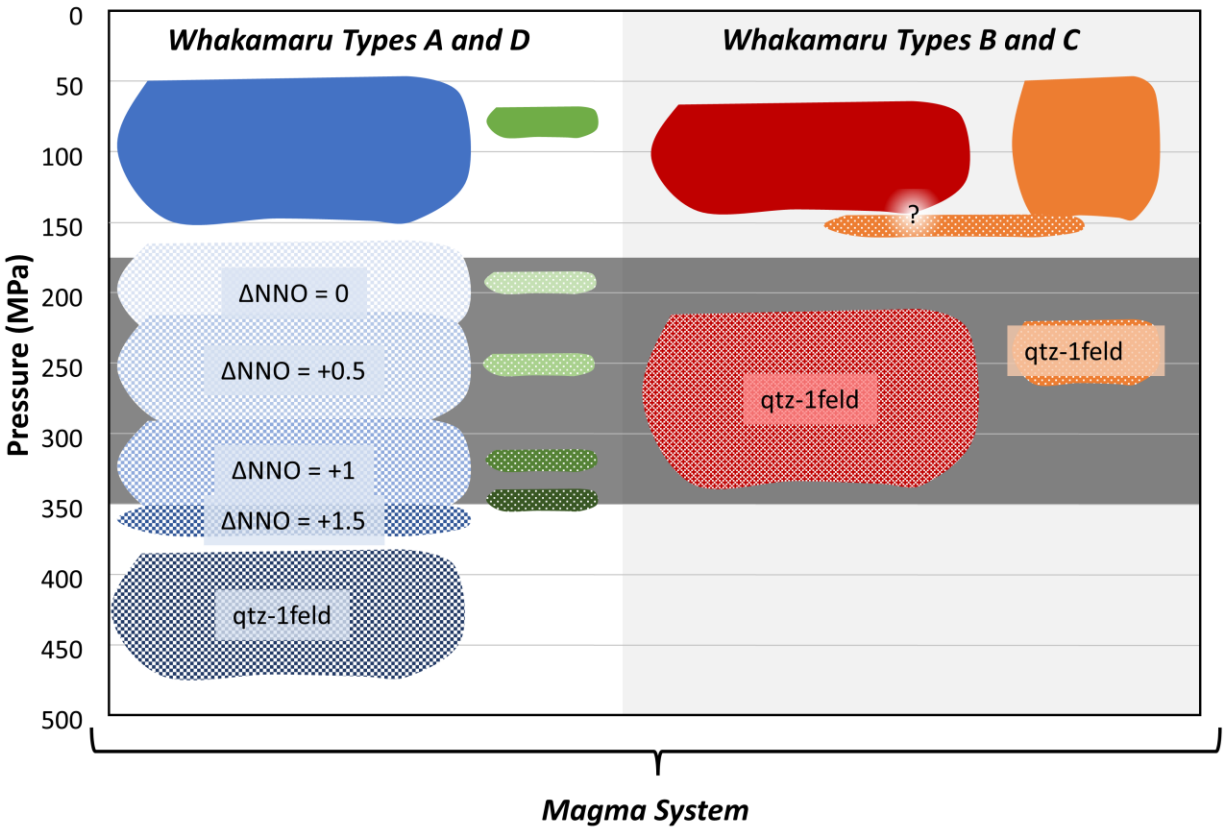

Figure 10 Schematic of melt-dominated magma bodies and magma mush bodies that constituted the Whakamaru magma system. The melt-dominated magma bodies were stored at shallow storage pressures (~50-150 MPa) and are represented by solid colors. The four magma types represent at least four different magma bodies. It is as yet unclear if type A and C magmas had additional, minor, shallower magma bodies at ~ 50 MPa. The textured magma bodies represent the magma mush bodies, from which the melt-dominated magmas were extracted. From the extraction assemblages and compositions of the pumice clasts, types A and D were part of one magma subsystem with an extraction assemblage of feld-opx±qtz, and types B and C were part of different subsystem with an extraction assemblage of qtz-1feld. The extraction pressures for types A and D are dependent on f_{O2}, with the shallower magma mush body representative of a lower f_{O2}, and

the deeper extraction depth representing a higher f_{O2} and a feld-opx±qtz extraction assemblage. Independent f_{O2} estimates indicate that an f_{O2} of ΔNNO = ~+0.5 to +1 are most likely (Matthews, 2011). For types B and C, only the qtz-1feld extraction assemblage gives valid extraction pressures. The most likely extraction pressure is highlighted in dark gray (~175-350 MPa). All four magma types experienced non-contiguous extraction and storage. There is a possibility that a portion of type C magma also experienced contiguous extraction and storage, represented by the highlighted question mark and discussed in the text.

The timing of the Whakamaru eruptions

Understanding the temporal relations of the Whakamaru group ignimbrites is difficult given the lack of distinctive field relationships between the different ignimbrites (Briggs, 1976a, 1976b; Brown *et al.*, 1998; Leonard *et al.*, 2010; Wilson *et al.*, 1986). However, we can take advantage of pyroclastic fall deposits from the Kohioawa and Ōtarawairere locations in the Bay of Plenty (Figure 2) that have been correlated to the Whakamaru group ignimbrites (Manning, 1995, 1996; Harmon *et al.*, Part 1) to constrain the relative timing of the ignimbrites by matching magma types, mineralogy, and glass compositions from the tephra with the characteristics of the ignimbrites. Evidence from the tephra shows that there are three main phases of the Whakamaru eruptions (Harmon *et al.*, Part 1):

1. In the initial stages of the Whakamaru eruptions, tephra deposits show exclusively type A pumice, likely from one melt-dominated magma body. The initial stages of the eruption being sourced by only type A magma is supported by a lack of sanidine in the lowest drill core data from Whakamaru ignimbrite deposits (Ewart, 1965; Martin, 1965; Grindley, 1965; Ewart & Healy, 1966), which has been interpreted as the first pulse of ignimbrite

eruption, and correlates to the widespread Rangitawa tephra (Pillans *et al.*, 1996; Matthews *et al.*, 2012c) and the base of the Whakamaru tephra sequence (i.e. Kohioawa tephra sequence) in the Bay of Plenty (Harmon *et al.*, Part 1).

2. Both magma types A and B are found in the next tephra package at Kohioawa and Ōtarawairere (Harmon *et al.*, Part 1), which is the thickest and is massive. This indicates that two magma types from at least two distinct, melt-dominated magma bodies erupted through the majority of the Whakamaru eruptions. From both the ignimbrite mineralogy by Brown *et al.* (1998) and from the mineralogy identified in the tephra horizons and inferred by rhyolite-MELTS for the correlative tephras (Harmon *et al.*, Part 1) and ignimbrites (this study), type B magma is shown to be saturated in sanidine (qtz-2feld storage pressures), while type A is sanidine-absent, further confirming the presence of the two separate, melt-dominated magma bodies.
3. Type C pumice is only present in the upper correlative tephra unit. It is marked by a change in field characteristics from massive to interbedded fine and coarse layers that contain clasts with glass from types A, B, and C, with most of the clasts exhibiting type C glass compositions (Harmon *et al.*, Part 1). This suggests mobilization of three melt-dominated magma bodies (types A, B, and C) in the final stages of the Whakamaru eruptions as recorded by the Kohioawa tephra sequence. Any ignimbrite that contains type C pumice must be a later erupted unit.

To summarize, type A continuously erupts throughout the Whakamaru eruptions, while type B appears in the second and third Kohioawa tephra units. Type C is a late-erupted magma type that only erupts in the third unit of the tephras – it is the dominant magma type at that stage.

Since we cannot distinguish type A from type D using only glass compositions, we cannot determine where in the stratigraphy type D magma erupts.

Since evidence from the tephra deposits requires that no sanidine-bearing magma be erupted in the beginning of the eruptions, only types A and D can erupt in the first phase (Harmon *et al.*, Part 1). Since the Rangitaiki ignimbrite exhibits only type A (Brown, 1994; Brown *et al.*, 1998; Matthews, 2011), it is most likely erupted early in the sequence. This implies that the Rangitaiki ± Te Whaiti ignimbrites preserved in the east likely erupted first due to the lack of sanidine and confirms the Wilson *et al.* (1986) interpretation that the Te Whaiti was part of the earliest eruptions. However, more evidence from the Te Whaiti deposits is required to definitively interpret the deposits as the first ignimbrites of the sequence. There are also several outcrops from the Whakamaru ignimbrite (including the samples from unknown Whakamaru ignimbrite locations), that contain exclusively type A pumice clasts, which is consistent with the base of the Whakamaru drill core lacking sanidine (Brown *et al.*, 1998; Grindley, 1965; Ewart & Healy, 1966). There are likely earlier eruptive pulses to the west as well as the east, although we note there are relatively few (<5) pumice clasts from each of these type A-only outcrops to the west from this study, which may not be representative of the pumice types present at these locations. In these locations, it is possible that these pulses of Whakamaru ignimbrite are correlative with the earliest eruptive phase.

The middle tephra package has clasts of types A and B compositions but no type C compositions (Harmon *et al.*, Part 1). The western Whakamaru ignimbrite deposits exhibit types A, B, and D, with no type C pumice clasts (Figure 6), indicating that these ignimbrite deposits correlate to the middle (and main pulse of) Whakamaru eruptions.

Clasts with type C magmas are only found in the upper tephra package (Harmon *et al.*, Part 1). Both the Manunui ignimbrite in the southwest and the Whakamaru ignimbrite in the northernmost samples on the west side of the TVZ (the Kinleith forest area) contain type C pumice. Due to the variation in pumice preservation, the Kinleith forest is where we collected the majority of the ignimbrite pumice clasts for this study (Figures 2 and 6). There is a large abundance of type C pumice in several Kinleith sampling locations, indicating that the northeast portion of the Kinleith area is likely one of the later erupted packages, representing the youngest pulses of the Whakamaru ignimbrite. The somewhat narrow geographic range of type C in the Whakamaru ignimbrite suggests that its eruption is somewhat restricted in both time and space (Figure 6). This final phase of ignimbrite-forming eruptions likely had multiple pulses, as seen in the interbedded morphology of the tephras (Harmon *et al.*, Part 1).

To further decipher the timing of the Whakamaru eruptions, mineral and bulk ignimbrite analyses could be performed. The thicker section of Whakamaru ignimbrite (e.g., at the Maraetai dam, see Ewart, 1965; Martin, 1965; Brown *et al.*, 1998) should be analyzed to determine at what stratigraphic level type C appears within the Whakamaru ignimbrite.

The Kohioawa tephra deposits show the chronology of the eruptions, and the ignimbrites provide additional compositional information. Together, this provides a time-integrated view of the magma system, including the melt-dominated magma bodies, magma mush bodies, and the timing of eruptions. While ~40 samples are a tiny minority of the erupted material (>2000 km^3 DRE), it is the combination with the tephra data that allows us to constrain the timing of the ignimbrites that has eluded previous researchers.

The Whakamaru Magma System

We demonstrate the presence of two independent magma subsystems that comprise the Whakamaru magma system – one subsystem is responsible for the types A and D magmas, and the other is linked to types B and C magmas. Results for types A, B, and D indicate non-contiguous storage and require that magmas be extracted and subsequently migrated up through the crust away from the mush; for type C, one sample (WHA039J) shows similar storage and extraction pressures, suggesting that contiguous extraction and storage is a possibility for some type C magmas. We show evidence that the Whakamaru magma system is vertically extensive and the glass compositions, storage temperatures, and storage pressures further suggest that the different magma types were likely independent, adjacent melt-dominated magma bodies (Figures 9 and 10).

The relationship between type B and type C magmas is potentially illuminated by the extraction pressures (Figures 7 and 10). The type C pumice clasts have extraction pressures that partly overlap with type B extraction pressures, but which also extend to shallower pressures that overlap with the type B storage pressures, particularly when considering the storage pressures from both the ignimbrites (this study) and the Kohioawa tephras (Harmon *et al.*, Part 1) in combination (Figure 9). It is possible that there is a vertically extensive magma mush system sourcing the type B and type C magmas, where some of the type C magma is extracted from a type B mush at the base of the type B melt-dominated magma body. Since type C is erupted only in the final tephra unit, it is possible that the more evolved, lower Ba and Sr concentrations are a consequence of extraction from the type B magma body following crystallization of two feldspars, as the glass compositions of type B overlap with the whole-rock compositions of type C (Figures 5 and 8). The similarity in the whole-rock and glass compositions, mineral

assemblages, and extraction pressures indicates that types B and C are likely geochemically related to the same source. However, the slight differences in whole-rock and glass compositions show that the more evolved signature for type C could indicate that it is extracted from type B in a two-part extraction and storage. This could be both a temporal and/or spatial relationship. This is consistent with observations from the tephra sequences, which show that type C magmas only appear late in the erupted sequence (Harmon *et al.*, Part 1).

The overlapping storage pressures of the different magma types – both from this study and from Harmon *et al.* (Part 1) – indicate that the system does not include a single, vertically-zoned magma chamber as proposed by Brown *et al.* (1998). Instead, it is more likely to consist of multiple, adjacent melt-dominated magma bodies. Due to the uncertainties in storage pressure, it is possible, but unlikely, that the magma bodies of different types overlap and mix. Since the Whakamaru and Manunui ignimbrites both contain multiple pumice types, often found in the same outcrop, the compositionally distinct, melt-dominated magma bodies must have coexisted in the crust prior to eruption. Therefore, a single magma body cannot have sourced the Whakamaru group eruptions. Further, the extraction of magma from the two magma subsystems indicates that the Whakamaru system was complex, with multiple sources of melt-dominated magma. Combining the evidence from the ignimbrites (this study) and correlated tephras (Harmon *et al.*, Part 1), we conclude that the two subsystems (A+D and B+C) existed for most or all of the eruptive history of the Whakamaru group of eruptions.

CONCLUSIONS

In this study, we use matrix-glass and whole-rock compositions of pumice from the Whakamaru group ignimbrites to determine the chemical variability of the magmas erupted, the pressures of magma storage and extraction, and combine evidence from pyroclastic fall material

to determine the timing of the eruptions of the different ignimbrites (Harmon *et al.*, Part 1). We find that there are four magma types (types A, B, C, D – confirming the conclusions of Brown *et al.* (1998). Using matrix glass and whole-rock compositional pairs from pumice clasts from the Whakamaru ignimbrite, we find that all magmas were saturated in zircon and that only magma types B and C were saturated in sanidine. The four different types of magma were likely stored in four independent magma bodies laterally juxtaposed to one another in the upper crust (~ 50-150 MPa).

Differences in extraction conditions indicate that the Whakamaru magma system is composed of two magma subsystems - one sourced magma types A + D and the other sourced magma types B + C. The two subsystems have either different magma mush extraction assemblages (orthopyroxene + feldspar for the subsystem that produced types A +D vs. feldspar + quartz for the subsystem that produced types B + C) or different extraction pressures (deeper for the subsystem that produced types A + D vs. shallower for the subsystem that produced types B + C). Evidence from SiO_2 compositions indicates that the first option is more likely and that magma from the two subsystems was extracted from a constricted crustal range (~ 175-350) with a differing mineral assemblage (Figure 10). The consistent shallow magma body storage pressures and likely constrained extraction pressures indicate a possible tectonic or structural control on where the melt-dominated magma bodies were extracted and subsequently stored prior to eruption.

There has been substantial debate about the timing of the different eruptions. Using the co-erupted tephras (Harmon *et al.*, Part 1), we hypothesize that the Te Whaiti and Rangitaiki ignimbrites to the east of the Whakamaru caldera erupted first, before the Manunui and Whakamaru eruptions erupted to the west of the Whakamaru caldera in a later stage. The final

stages of the Whakamaru group ignimbrites are to the northwest, in the Kinleith forest area, where type C magma proliferates.

Using petrological and volcanological data from the ignimbrites and the associated tephras indicates that the Whakamaru magma system was sourced by two subsystems comprised of both magma mush bodies and melt-dominated magma bodies. These bodies were likely stored at overlapping depths spanning large swaths of the upper crust, although there were likely regions where little to no magma existed. It is only with the combination of data from the spatial distribution of the ignimbrites and the chronology of the tephras that we are able to understand how the Whakamaru group eruptions were extracted, stored, and erupted.

ACKNOWLEDGEMENTS

We would like to thank Calvin Miller, Mark Ghiorso, and Chad Deering for their assistance throughout the project. We thank the support from National Science Foundation 1714025, EAR-1151337, EAR-1830122 and from Vanderbilt University Discovery Grant.

DATA AVAILABILITY STATEMENT

The quantitative data underlying this article are available in the article and in its online supplementary material. SEM BSE images of clasts will be shared on reasonable request to the corresponding author.

REFERENCES

Allan, A. S. R., Morgan, D. J., Wilson, C. J. N. & Millet, M. A. (2013). From mush to eruption in centuries: Assembly of the super-sized Oruanui magma body. *Contributions to Mineralogy and Petrology* **166**, 143–164.

Allan, A.S.R., Barker, S.J., Millet, M.A., Morgan, D.J., Rooyakkers, S.M., Schipper, C.I., and Wilson, C.J.N. (2017). A cascade of magmatic events during the assembly and eruption of a super-sized magma body. *Contributions to Mineralogy and Petrology* **172**, 49.

Annen, C., Blundy, J. D., Leuthold, J. & Sparks, R. S. J. (2015). Construction and evolution of igneous bodies: Towards an integrated perspective of crustal magmatism. *Lithos*. Elsevier **230**, 206–221.

Bachmann, O. & Bergantz, G. (2008). The magma reservoirs that feed supereruptions. *Elements* **4**, 17–21.

Bachmann, O. & Bergantz, G. W. (2004). On the origin of crystal-poor rhyolites: Extracted from batholithic crystal mushes. *Journal of Petrology* **45**, 1565–1582.

Bachmann, O. & Huber, C. (2016). Silicic magma reservoirs in the Earth's crust. *American Mineralogist* **101**, 2377–2404.

Barboni, M. & Schoene, B. (2014). Short eruption window revealed by absolute crystal growth rates in a granitic magma. *Nature Geoscience* **7**, 524–528.

Bégué, F., Deering, C. D., Gravley, D. M., Kennedy, B. M., Chambefort, I., Gualda, G. A. R. & Bachmann, O. (2014a). Extraction, storage and eruption of multiple isolated magma batches in the paired Mamaku and Ohakuri eruption, Taupo Volcanic Zone, New Zealand. *Journal of Petrology* **55**, 1653–1684.

952 Bégué, F., Gualda, G. A. R., Ghiorso, M. S., Pamukçu, A. S., Kennedy, B. M., Gravley, D.
953 M., Deering, C. D. & Chambefort, I. (2014b). Phase-equilibrium geobarometers for
954 silicic rocks based on rhyolite-MELTS. Part 2: application to Taupo Volcanic Zone
955 rhyolites. *Contributions to Mineralogy and Petrology* **168**, 1–16.
956 Bindeman, I. N. & Valley, J. W. (2003). Rapid generation of both high- and low-delta18O,
957 large-volume silicic magmas at the Timber Mountain/Oasis Valley caldera complex,
958 Nevada. *GSA Bulletin* **10**, 581–595.
959 Blundy, J. (2022). Chemical Differentiation by Mineralogical Buffering in Crustal Hot
960 Zones. *Journal of Petrology*. **63**, egac054.
961 Blundy, J. D. & Cashman, K. V. (2008). Petrologic reconstruction of magmatic system
962 variables and processes. *Reviews in Mineralogy and Geochemistry* **69**, 179–239.
963 Boehnke, P., Watson, E. B., Trail, D., Harrison, T. M. & Schmitt, A. K. (2013). Zircon
964 saturation re-revisited. *Chemical Geology* **351**, 324–334.
965 Briggs, N. D. (1976a). Welding and crystallisation zonation in Whakamaru ignimbrite,
966 central North Island, New Zealand. *New Zealand Journal of Geology and Geophysics*
967 **19**, 189–212.
968 Briggs, N. D. (1976b). Recognition and correlation of subdivisions within the Whakamaru
969 ignimbrite, central North Island, New Zealand. *New Zealand Journal of Geology and*
970 *Geophysics* **19**, 463–501.
971 Brown, S. J. A. (1994). Geology and geochemistry of the Whakamaru Group ignimbrites,
972 and associated rhyolite domes, Taupo Volcanic Zone, New Zealand. Christchurch,
973 University of Canterbury.

Brown, S. J. A. & Fletcher, I. R. (1999). SHRIMP U-Pb dating of the preeruption growth history of zircons from the 340 ka Whakamaru Ignimbrite, New Zealand: Evidence for >250 k.y. magma residence times. *Geology* **27**, 1035–1038.

Brown, S. J. A., Wilson, C. J. N., Cole, J. W. & Wooden, J. L. (1998). The Whakamaru group ignimbrites, Taupo Volcanic Zone, New Zealand: Evidence for reverse tapping of a zoned silicic magmatic system. *Journal of Volcanology and Geothermal Research* **84**, 1–37.

Cashman, K. V. & Giordano, G. (2014). Calderas and magma reservoirs. *Journal of Volcanology and Geothermal Research* **288**, 28–45.

Cashman, K. V., Stephen, R., Sparks, J. & Blundy, J. D. (2017). Vertically extensive and unstable magmatic systems: A unified view of igneous processes. *Science* **355**, eaag3055.

Chakraborty, S. & Dohmen, R. (2022). Diffusion chronometry of volcanic rocks: looking backward and forward. *Bulletin of Volcanology* **84**, 57.

Chambefort, I., Lewis, B., Wilson, C. J. N., Rae, A. J., Coutts, C., Bignall, G. & Ireland, T. R. (2014). Stratigraphy and structure of the Ngatamariki geothermal system from new zircon U–Pb geochronology: Implications for Taupo Volcanic Zone evolution. *Journal of Volcanology and Geothermal Research* **274**, 51–70.

Chamberlain, K. J., Wilson, C. J. N., Wallace, P. J. & Millet, M. A. (2015). Micro-analytical perspectives on the Bishop Tuff and its magma chamber. *Journal of Petrology* **56**, 605–640.

Chamberlain, K. J., Wilson, C. J. N., Wooden, J. L., Charlier, B. L. A. & Ireland, T. R. (2014). New perspectives on the Bishop Tuff from zircon textures, ages and trace elements. *Journal of Petrology* **55**, 395–426.

Charlier, B. L. A., Bachmann, O., Davidson, J. P., Dungan, M. A. & Morgan, D. J. (2007). The upper crustal evolution of a large silicic magma body: Evidence from crystal-scale Rb - Sr isotopic heterogeneities in the fish canyon magmatic system, Colorado. *Journal of Petrology* **48**, 1875–1894.

Charlier, B. L. A., Wilson, C. J. N. & Davidson, J. P. (2008). Rapid open-system assembly of a large silicic magma body: Time-resolved evidence from cored plagioclase crystals in the Oruanui eruption deposits, New Zealand. *Contributions to Mineralogy and Petrology* **156**, 799–813.

Cooper, G. F., Morgan, D. J. & Wilson, C. J. N. (2017). Rapid assembly and rejuvenation of a large silicic magmatic system: Insights from mineral diffusive profiles in the Kidnappers and Rocky Hill deposits, New Zealand. *Earth and Planetary Science Letters* **473**, 1–13.

Cooper, G. F., Wilson, C. J. N., Millet, M. A., Baker, J. A. & Smith, E. G. C. (2012). Systematic tapping of independent magma chambers during the 1Ma Kidnappers supereruption. *Earth and Planetary Science Letters* **313–314**, 23–33.

Cooper, K. M. & Kent, A. J. R. (2014). Rapid remobilization of magmatic crystals kept in cold storage. *Nature* **506**, 480–483.

Deering, C. D., Bachmann, O. & Vogel, T. A. (2011). The Ammonia Tanks Tuff: Erupting a melt-rich rhyolite cap and its remobilized crystal cumulate. *Earth and Planetary Science Letters* **310**, 518–525.

1018 Deering, C. D., Gravley, D. M., Vogel, T. A., Cole, J. W. & Leonard, G. S. (2010). Origins
1019 of cold-wet-oxidizing to hot-dry-reducing rhyolite magma cycles and distribution in
1020 the Taupo Volcanic Zone, New Zealand. *Contributions to Mineralogy and Petrology*
1021 **160**, 609–629.
1022 Downs, D. T., Wilson, C. J. N., Cole, J. W., Rowland, J. V., Calvert, A. T., Leonard, G. S.
1023 & Keall, J. M. (2014). Age and eruptive center of the Paeroa Subgroup ignimbrites
1024 (Whakamaru Group) within the Taupo Volcanic Zone of New Zealand. *Bulletin of the*
1025 *Geological Society of America* **126**, 1131–1144.
1026 Druitt, T. H., Costa, F., Deloule, E., Dungan, M. & Scaillet, B. (2012). Decadal to monthly
1027 timescales of magma transfer and reservoir growth at a caldera volcano. *Nature* **482**,
1028 77–80.
1029 Eastwood, A. A., Gravley, D. M., Wilson, C. J. N., Chambefort, I., Oze, C., Cole, J. W. &
1030 Ireland, T. R. (2013). U-Pb dating of subsurface pyroclastic deposits (Tahorakuri
1031 Formation) at Ngatamariki and Rotokawa Geothermal Fields. *35th New Zealand*
1032 *Geothermal Workshop*. Rotorua, New Zealand.
1033 Ewart, A. (1965). Mineralogy and petrogenesis of the Whakamaru Ignimbrite in the
1034 Maraetai area of the Taupo Volcanic Zone, New Zealand. *New Zealand Journal of*
1035 *Geology and Geophysics* **8**, 611–679.
1036 Ewart, A. (1967a). The Petrography of the Central North Island rhyolitic lavas. *New*
1037 *Zealand Journal of Geology and Geophysics* **10**, 182–197.
1038 Ewart, A. (1967b). Pyroxene and magnetite phenocrysts from the Taupo quaternary
1039 rhyolitic pumice deposits, New Zealand. *Mineralogy Magazine* **36**, 180–194.

Ewart, A. & Healy, J. (1966). Te Whaiti ignimbrites at Murupara. In: Thompson, B., Kermode, L. & Ewart, A. (eds) *New Zealand Volcanology, Central Volcanic Region*. New Zealand Department of Scientific and Industrial Research Information, 121–125.

Fabbro, G. N., Druitt, T. H. & Costa, F. (2017). Storage and eruption of silicic magma across the transition from dominantly effusive to caldera-forming states at an arc volcano (Santorini, Greece). *Journal of Petrology*. **58**, 2429–2464.

Foley, M. L., Miller, C. F. & Gualda, G. A. R. (2020). Architecture of a super-sized magma chamber and remobilization of its basal cumulate (Peach Spring Tuff, USA). *Journal of Petrology* **61**, egaa020.

Ghiorso, M. S. & Gualda, G. A. R. (2015). An H_2O–CO_2 mixed fluid saturation model compatible with rhyolite-MELTS. *Contributions to Mineralogy and Petrology* **169**, 53.

Ghiorso, M. S., Matthews, S. & Sverjensky, D. A. (2023). MELTS+DEW: Modeling major element+Cl+F+S phase equilibria, redox reactions and elemental partitioning in magmatic-hydrothermal systems. Lyon: Goldschmidt.

Giordano, G. & Caricchi, L. (2022). Determining the state of activity of transcrustal magmatic systems and their volcanoes. *Annual Review of Earth and Planetary Sciences* **50**, 231–259.

Gravley, D. M., Deering, C. D., Leonard, G. S. & Rowland, J. V. (2016). Ignimbrite flare-ups and their drivers: A New Zealand perspective. *Earth-Science Reviews* **162**, 65–82.

Gravley, D. M., Wilson, C. J. N., Leonard, G. S. & Cole, J. W. (2007). Double trouble: Paired ignimbrite eruptions and collateral subsidence in the Taupo Volcanic Zone, New Zealand. *Bulletin of the Geological Society of America* **119**, 18–30.

Griffin, W., Powell, W., Pearson, N. J. & O'Reilly, S. (2008). GLITTER: data reduction software for laser ablation ICP-MS. *Short Course Series* **40**, 308–311.

Grindley, G. W. (1960). Geological Map of New Zealand 1:250,000. *NZ Department of Scientific and Industrial Research*. Wellington, New Zealand.

Grindley, G.W. (1965). The geology, structure, and exploitation of the Wairakei Geothermal Field, Taupo, New Zealand. *New Zealand Geological Society Bulletin* **75**, 131.

Gualda, G. A. R. & Ghiorso, M. S. (2013a). Low-pressure origin of high-silica rhyolites and granites. *The Journal of Geology* **121**, 537–545.

Gualda, G. A. R. & Ghiorso, M. S. (2013b). The Bishop Tuff giant magma body: an alternative to the Standard Model. *Contributions to Mineralogy and Petrology* **166**, 755–775.

Gualda, G. A. R. & Ghiorso, M. S. (2014). Phase-equilibrium geobarometers for silicic rocks based on rhyolite-MELTS. Part 1: Principles, procedures, and evaluation of the method. *Contributions to Mineralogy and Petrology* **168**, 1–17.

Gualda, G. A. R., Ghiorso, M. S., Hurst, A. A., Allen, M. C. & Bradshaw, R. W. (2022). A complex patchwork of magma bodies that fed the Bishop Tuff supereruption (Long Valley Caldera, CA, United States): Evidence from matrix glass major and trace-element compositions. *Frontiers in Earth Science* **10**.

Gualda, G. A. R., Ghiorso, M. S., Lemons, R. V. & Carley, T. L. (2012a). Rhyolite-MELTS: a Modified Calibration of MELTS Optimized for Silica-rich, Fluid-bearing Magmatic Systems. *Journal of Petrology* **53**, 875–890.

1084 Gualda, G. A. R., Gravley, D. M., Conner, M., Hollmann, B., Pamukçu, A. S., Bégué, F.,
1085 Ghiorso, M. S. & Deering, C. D. (2018). Climbing the crustal ladder: Magma storage-
1086 depth evolution during a volcanic flare-up. *Science Advances* **4**, eaap7567.
1087 Gualda, G. A. R., Gravley, D. M., Deering, C. D. & Ghiorso, M. S. (2019). Magma
1088 extraction pressures and the architecture of volcanic plumbing systems. *Earth and*
1089 *Planetary Science Letters* **522**, 118–124.
1090 Gualda, G. A. R., Pamukçu, A. S., Ghiorso, M. S., Anderson Jr, A. T., Sutton, S. R., Rivers,
1091 M. L. & Houlie, N. (2012b). Timescales of quartz crystallization and the longevity of
1092 the Bishop giant magma body. *PLoS ONE* **7**, e37492.
1093 Gualda, G. A. R. & Sutton, S. R. (2016). The year leading to a supereruption. *PLoS ONE*
1094 **11**, 1–18.
1095 Hansteen, T. H. & Klügel, A. (2008). Fluid inclusion thermobarometry as a tracer for
1096 magmatic processes. *Reviews in Mineralogy and Geochemistry* **69**, 143–177.
1097 Harmon, L. J., Cowlyn, J., Gualda, G. A. R. & Ghiorso, M. S. (2018). Phase-equilibrium
1098 geobarometers for silicic rocks based on rhyolite-MELTS. Part 4: Plagioclase,
1099 orthopyroxene, clinopyroxene, glass geobarometer, and application to Mt. Ruapehu,
1100 New Zealand. *Contributions to Mineralogy and Petrology* **173**, 7.
1101 Harmon, L. J., Gualda, G. A. R., Gravley, D. M., Smithies, S. L., Deering, C. D.
1102 (submitted). The Whakamaru Magmatic System (Taupō Volcanic Zone, New
1103 Zealand), Part 1: Evidence from tephra deposits for the eruption of multiple magma
1104 types through time. *Journal of Volcanology and Geothermal Research*.
1105 Harper, B. E., Miller, C. F., Koteas, G. C., Cates, N. L., Wiebe, R. A., Lazzareschi, D. S. &
1106 Cribb, J. W. (2004). Granites, dynamic magma chamber processes and pluton

construction: the Aztec Wash pluton, Eldorado Mountains, Nevada, USA. *Earth and Environmental Science Transactions of The Royal Society of Edinburgh* **95**, 277–295.

Harrison, A. & White, R. S. (2006). Lithospheric structure of an active backarc basin: The Taupo Volcanic Zone, New Zealand. *Geophysical Journal International* **167**, 968–990.

Hildreth, W. (1979). The Bishop Tuff: Evidence for the origin of compositional zonation in silicic magma chambers. *Geological Society of America Special Paper* **180**, 43-75.

Hildreth, W. (2004). Volcanological perspectives on Long Valley, Mammoth Mountain, and Mono Craters: Several contiguous but discrete systems. *Journal of Volcanology and Geothermal Research* **136**, 169–198.

Hildreth, W. & Wilson, C. J. N. (2007). Compositional zoning of the Bishop Tuff. *Journal of Petrology* **48**, 951–999.

Hilley, G. E. (ed.), Brodsky, E. E., Roman, D., Shillington, D. J., Brudzinski, M., Behn, M., Tobin, H. & the SZ4D RCN (2022). SZ4D Implementation Plan. *Stanford Digital Repository*.

Houghton, B. F., Wilson, C. J. N., McWilliams, M. O., Lanphere, M. A., Weaver, S. D., Briggs, R. M. & Pringle, M. S. (1995). Chronology and dynamics of a large silicic magmatic system: Central Taupo Volcanic Zone, New Zealand. *Geology* **23**, 13–16.

Iacovino, K., Matthews, S., Wieser, P. E., Moore, G. M. & Bégué, F. (2021). VESIcal Part I: An Open-Source Thermodynamic Model Engine for Mixed Volatile (H_2O-CO_2) Solubility in Silicate Melts. *Earth and Space Science* **8**, e2020EA001584.

Jochum, K. P., Weis, U., Schwager, B., Stoll, B., Wilson, S. A., Haug, G. H., Andreae, M. O. & Enzweiler, J. (2016). Reference values following ISO guidelines for frequently

requested rock reference materials. *Geostandards and Geoanalytical Research* **40**, 333–350.

Karakas, O., Degruyter, W., Bachmann, O. & Dufek, J. (2017). Lifetime and size of shallow magma bodies controlled by crustal-scale magmatism. *Nature Geoscience* **10**, 446–450.

Kelley, K. A. & Cottrell, E. (2009). Water and the oxidation state of subduction zone magmas. *Science* **325**, 605–607.

Leonard, G. S., Begg, J. G. & Wilson, C. J. N. (2010). Geology of the Rotorua area. Lower Hutt, New Zealand: GNS Science.

Manning, D. A. (1995). Late Pleistocene tephrostratigraphy of the Eastern Bay of Plenty region, New Zealand. Wellington, Victoria University.

Manning, D. A. (1996). Middle-late Pleistocene tephrostratigraphy of the eastern Bay of Plenty, New Zealand. *Quaternary International* **34–36**, 3–12.

Martin, R. C. (1961). Stratigraphy and structural outline of the Taupo Volcanic Zone. *New Zealand Journal of Geology and Geophysics* **4**, 449–478.

Martin, R. C. (1965). Lithology and eruptive history of the Whakamaru ignimbrites in the Maraetai area of the Taupo volcanic zone, New Zealand. *New Zealand Journal of Geology and Geophysics* **8**, 680–705.

Matthews, N. E. (2011). Magma chamber assembly and dynamics of a supervolcano: Whakamaru, Taupo Volcanic Zone, New Zealand. Oxford, University of Oxford.

Matthews, N. E., Huber, C., Pyle, D. M. & Smith, V. C. (2012a). Timescales of magma recharge and reactivation of large silicic systems from Ti diffusion in quartz. *Journal of Petrology* **53**, 1385–1416.

Matthews, N. E., Pyle, D. M., Smith, V. C., Wilson, C. J. N., Huber, C. & van Hinsberg, V. (2012b). Quartz zoning and the pre-eruptive evolution of the ~340-ka Whakamaru magma systems, New Zealand. *Contributions to Mineralogy and Petrology* **163**, 87–107.

Matthews, N. E., Smith, V. C., Costa, A., Durant, A. J., Pyle, D. M. & Pearce, N. J. G. (2012c). Ultra-distal tephra deposits from super-eruptions: Examples from Toba, Indonesia and Taupo Volcanic Zone, New Zealand. *Quaternary International* **258**, 54–79.

Moore, G., Vennemann, T. & Carmichael, I. S. E. (1998). An empirical model for the solubility of H_2O in magmas to 3 kilobars. *American Mineralogist* **83**, 36–42.

Pamukçu, A. S., Carley, T. L., Gualda, G. A. R., Miller, C. F. & Ferguson, C. A. (2013). The evolution of the peach spring giant magma body: Evidence from accessory mineral textures and compositions, bulk pumice and glass geochemistry, and rhyolite-MELTS modeling. *Journal of Petrology* **54**, 1109–1148.

Pamukçu, A. S., Gualda, G. A. R., Bégué, F. & Gravley, D. M. (2015a). Melt inclusion shapes: Timekeepers of short-lived giant magma bodies. *Geology* **43**, 947–950.

Pamukçu, A. S., Gualda, G. A. R., Ghiorso, M. S., Miller, C. F. & McCracken, R. G. (2015b). Phase-equilibrium geobarometers for silicic rocks based on rhyolite-MELTS—Part 3: Application to the Peach Spring Tuff (Arizona–California–Nevada, USA). *Contributions to Mineralogy and Petrology* **169**, 1-17.

Pamukçu, A. S., Gualda, G. A. R. & Gravley, D. M. (2021). Rhyolite-MELTS and the storage and extraction of large-volume crystal-poor rhyolitic melts at the Taupō

Volcanic Center: a reply to Wilson *et al.* (2021). *Contributions to Mineralogy and Petrology* **176**, 1-16.

Papale, P., Moretti, R. & Barbato, D. (2006). The compositional dependence of the saturation surface of H_2O + CO_2 fluids in silicate melts. *Chemical Geology* **229**, 78–95.

Pearce, N. J. G., Westgate, J. A., Gualda, G. A. R., Gatti, E. & Muhammad, R. F. (2020). Tephra glass chemistry provides storage and discharge details of five magma reservoirs which fed the 75 ka Youngest Toba Tuff eruption, northern Sumatra. *Journal of Quaternary Science* **35**, 256–271.

Pelullo, C., Iovine, R. S., Arienzo, I., Di Renzo, V., Pappalardo, L., Petrosino, P. & D'antonio, M. (2022). Mineral-melt equilibria and geothermobarometry of Campi Flegrei magmas: inferences for magma storage conditions. *Minerals* **12**, 108.

Pillans, B., Kohn, B. P., Berger, G., Froggatt, P., Duller, G., Alloway, B. & Hesset, P. (1996). Multi-method dating comparison for mid-Pleistocene Rangitawa Tephra, New Zealand. *Quaternary Science Reviews* **15**, 641–653.

Pitcher, B. W., Gualda, G. A. R. & Hasegawa, T. (2021). Repetitive Duality of Rhyolite Compositions, Timescales, and Storage and Extraction Conditions for Pleistocene Caldera-forming Eruptions, Hokkaido, Japan. *Journal of Petrology* **62**, egaa106.

Putirka, K. D. (2008). Thermometers and Barometers for Volcanic Systems. *Reviews in Mineralogy and Geochemistry* **69**, 61–120.

Reed, S. J. B. & Ware, N. G. (1973). Quantitative electron microprobe analysis using a lithium drifted silicon detector. *X-Ray Spectrometry* **2**, 69–74.

Reid, M. R. & Vazquez, J. A. (2017). Fitful and protracted magma assembly leading to a giant eruption, Youngest Toba Tuff, Indonesia. *Geochemistry Geophysics Geosystems* **18**, 156–177.

Ridolfi, F., Renzulli, A. & Puerini, M. (2010). Stability and chemical equilibrium of amphibole in calc-alkaline magmas: An overview, new thermobarometric formulations and application to subduction-related volcanoes. *Contributions to Mineralogy and Petrology* **160**, 45–66.

Ritchie, N. W. M., Newbury, D. E. & Davis, J. M. (2012). EDS Measurements of X-ray intensity at WDS precision and accuracy using a silicon drift detector. *Microscopy and Microanalysis* **18**, 892–904.

Saunders, K., Morgan, D. J., Baker, J. A. & Wysoczanski, R. J. (2010). The magmatic evolution of the Whakamaru supereruption, New Zealand, constrained by a microanalytical study of plagioclase and quartz. *Journal of Petrology* **51**, 2465–2488.

Shamloo, H. I. & Till, C. B. (2019). Decadal transition from quiescence to supereruption: petrologic investigation of the Lava Creek Tuff, Yellowstone Caldera, WY. *Contributions to Mineralogy and Petrology* **174**, 32.

Simon, J. I. & Reid, M. R. (2005). The pace of rhyolite differentiation and storage in an "archetypical" silicic magma system, Long Valley, California. *Earth and Planetary Science Letters* **235**, 123–140.

Smithies, S. L., Harmon, L. J., Allen, S. M., Gravley, D. M. & Gualda, G. A. R. (2023). Following magma: The pathway of silicic magmas from extraction to storage during an ignimbrite flare-up, Taupō Volcanic Zone, New Zealand. *Earth and Planetary Science Letters* **607**, 118053.

Sparks, R. S. J., Annen, C., Blundy, J. D., Cashman, K. V., Rust, A. C. & Jackson, M. D. (2019). Formation and dynamics of magma reservoirs. *Philosophical Transactions of the Royal Society A: Mathematical, Physical and Engineering Sciences* **377**, 20180019.

Stelten, M. E., Cooper, K. M., Vazquez, J. A., Calvert, A. T. & Glessner, J. J. G. (2014). Mechanisms and timescales of generating eruptible rhyolitic magmas at Yellowstone Caldera from Zircon and sanidine geochronology and geochemistry. *Journal of Petrology* **56**, 1607–1642.

Stern, T. A., Stratford, W. R. & Salmon, M. L. (2006). Subduction evolution and mantle dynamics at a continental margin: Central North Island, New Zealand. *Reviews of Geophysics* **44**, RG4002.

Swallow, E. J., Wilson, C. J. N., Myers, M. L., Wallace, P. J., Collins, K. S. & Smith, E. G. C. (2018). Evacuation of multiple magma bodies and the onset of caldera collapse in a supereruption, captured in glass and mineral compositions. *Contributions to Mineralogy and Petrology* **173**, 1–22.

Tavazzani, L., Peres, S., Sinigoi, S., Demarchi, G., Economos, R. C. & Quick, J. E. (2020). Timescales and Mechanisms of Crystal-mush Rejuvenation and Melt Extraction Recorded in Permian Plutonic and Volcanic Rocks of the Sesia Magmatic System (Southern Alps, Italy). *Journal of Petrology* **61**, egaa049.

van Achterbergh, E., Ryan, C. G., Jackson, S. E. & Griffin, W. L. (2001). Data reduction software for LAICPMS: appendix. In: Sylvester, P. J. (ed.) *Laser ablation ICPMS in the Earth Sciences: Principles and Applications*. Mineralogical Association of Canada Short Course Series, 224–239.

Wallrich, B. M., Miller, C. F., Gualda, G. A. R., Miller, J. S., Hinz, N. H. & Faulds, J. E. (2023). Volcano-pluton connection: Perspectives on material and process linkages, Searchlight pluton and Highland Range volcanic sequence, Nevada, USA. *Earth-Science Reviews* **238**, 104361.

Waters, L. E. & Lange, R. A. (2015). An updated calibration of the plagioclase-liquid hygrometer-thermometer applicable to basalts through rhyolites. *American Mineralogist* **100**, 2172–2184.

Watson, E. B. & Harrison, T. M. (1983). Zircon saturation revisited: temperature and composition effects in a variety of crustal magma types. *Earth and Planetary Science Letters* **64**, 295–304.

Weinberg, R. F., Vernon, R. H. & Schmeling, H. (2021). Processes in mushes and their role in the differentiation of granitic rocks. *Earth-Science Reviews* **220**, 103665.

Wiebe, R. A., Kolzenburg, S., Rooyakkers, S. M. & Stix, J. (2021). Plutonic record of a caldera-forming silicic eruption: The shatter zone of the Cadillac Mountain granite, coastal Maine. *Geosphere* **17**, 1–22.

Wieser, P. E., Iacovino, K., Matthews, S., Moore, G. & Allison, C. M. (2022). VESIcal: 2. A Critical Approach to Volatile Solubility Modeling Using an Open-Source Python3 Engine. *Earth and Space Science* **9**, e2021EA001932

Wilson, C. J. N. & Charlier, B. L. A. (2009). Rapid rates of magma generation at contemporaneous magma systems, Taupo Volcano, New Zealand: Insights from U-Th model-age spectra in Zircons. *Journal of Petrology* **50**, 875–907.

Wilson, C. J. N., Gravley, D. M., Leonard, G. S. & Rowland, J. V (2009). Volcanism in the central Taupo Volcanic Zone, New Zealand: tempo styles and controls. In: Thordarson,

T., Self, S., Larsen, G., Rowland, S. K. & Hoskuldsson, A. (eds) *Studies in Volcanology: The Legacy of George Walker. Special Publications of IAVCEI*, 225–247.

Wilson, C. J. N., Houghton, B. F. & Lloyd, E. F. (1986). Volcanic history and evolution of the Maroa-Taupo area. In: Smith, I. E. M. (ed.) *Late Cenozioc Volcanism in New Zealand*. Wellington: The Royal Society of New Zealand Bulletin **23**, 194–223.

Wilson, C. J. N., Houghton, B. F., McWilliams, M. O., Lanphere, M. A., Weaver, S. D. & Briggs, R. M. (1995). Volcanic and structural evolution of Taupo Volcanic Zone, New Zealand: a review. *Journal of Volcanology and Geothermal Research* **68**, 1–28.

Wilson, C. J. N., Rogan, A. M., Smith, I. E. M., Northey, D. J., Nairn, I. A. & Houghton, B. F. (1984). Caldera volcanoes of the Taupo volcanic zone, New Zealand. *Journal of Geophysical Research* **89**, 8463–8484.

Wolff, J. A. (2017). On the syenite-trachyte problem. *Geology*. **45**, 1067–1070.

TABLES

1. Description of the four ignimbrites (Whakamaru, Rangitaiki, Manunui, and Te Whaiti) from the literature, predominantly after Brown *et al.* (1998) and references therein.
2. Description of the four compositional types of rhyolite pumice (types A, B, C, and D) after Brown *et al.* (1998), Brown (1994), Matthews (2011), and Saunders *et al.* (2010).
3. Whole-rock compositional data and extraction pressure geobarometry results from pumice clasts from the Whakamaru group ignimbrites
4. Matrix glass compositional data, geothermometry results, and storage pressure geobarometry results from pumice clasts from the Whakamaru group ignimbrites

APPENDICES

1. Sample metadata, including sampling coordinates and analyses performed
2. USGS RGM standard major-element data for SEM-EDS

Table 1

Ignimbrite	General Location	Pumice Types Present	General Description
Whakamaru	west TVZ including Kinleith Forest	A, B, C, D	crystal rich texture; large, resorbed quartz; quartz-rich, welded ignimbrite lithic fragments; at the Maraetai Dam - increasing crystal content from 10-35+ wt% in lowest unit with increasing phenocryst size in upper units (units B-D); quartz-absent in lowest 30 m; size, abundance, and resorption of quartz increases with stratigraphic height; increase in biotite with biotite>hornblende at the top of the ignimbrite; opx present throughout ignimbrite; sanidine absent for base and units A-B; sanidine appears in units D-F; it is unclear if it's present in unit C
Manunui	west TVZ, further south	A, C, D	intensely welded, less crystal and pumice rich; metasedimentary lithic fragments present
Rangitaiki	east TVZ	A; Brown et al. (1998) notes that lack of biotite-rich Type B and C; Matthews (2011) finds one Rangitaiki pumice clast that has sanidine in thin section, but does not study it further (no XRF)	crystal rich texture; large, resorbed quartz; quartz-rich, welded ignimbrite lithic fragments; petrographically similar to Whakamaru ignimbrite; poorer in biotite than Whakamaru ignimbrite
Te Whaiti	east TVZ, further south	No unwelded pumice found	intensely welded, less crystal and pumice rich; metasedimentary lithic fragments

Table 2

Pumice Type	Crystallinity	Mineralogy	General Comments	WR SiO_2	WR Rb	WR Sr	WR K_2O/Na_2O	WR Ba
A	typically 30-40% but as low as 10%; plag are An25-35 with some An35-45 cores (< 6 mm) large, euhedral to subhedral, and complexly zoned, commonly intergrown, and twinned; qtz are large (< 12 mm) resorbed and rounded; opx to opx+hbl+bt in different pumice clasts - opx ubiquitous; bt higher Mg# than Type B and C (Mg# 47-50); mixing with basalt only in Type A	plag, qtz, opx, hbl, ± bt, mag/ilm	low silica rhyolite; high-Mg bt	70-74	80-140	140-200		750-1000
B	15-25% xtls; bt is predominant ferromag phase; san is Or68; qtz are smaller (< 3 mm), euhedral to subhedral, with less resorption than type A; plag smaller (< 3 mm), complexly zoned and twinned, commonly aggregates; bt less Mg-rich than Type A (Mg# 38.6-39.5)	plag, qtz, san, bt, mag ± hbl microlites	low-Mg bt; types B and C distinguishable in Rb and Sr; not easily distinguished in hand sample or thin section	>74	>120		K2O>Na2O	1000-1400
C	15-25% xtls; bt is predominant ferromag phase; san is Or68; qtz are smaller (< 3 mm), euhedral to subhedral, with less resorption than type A; plag dominant over qtz, smaller (< 3 mm), complexly zoned and twinned, commonly aggregates; bt less Mg-rich than Type A (Mg# 39); no hbl	qtz, plag, san, bt, mag, ilm	low Ba; bt rich; low-Mg bt	>75	>170		K2O > 4wt%	700-1000
D	30% xtls; plag-rich (21%), An25-35, large (< 4 mm), euhedral to subhedral, distinct melt inclusion at 0.1 - 0.3 mm from the xtl rim (resorption and regrowth), complexly zoned and twinned, forms in clusters; no plag-opx intergrowths (like in type A); qtz is subordinate (?) (5%), small (< 3 mm), strongly embayed to subhedral; no san; bt the main ferromag min; small amts of hbl and opx; bt similar Mg# to type A; elongate microlites of hbl and plag in matrix	plag, qtz, bt, hbl, opx	high Rb (>200 ppm); bt rich		~ 240	<155 (large range)		750-1000

Table 3

Sample Information			**Major-element whole-rock composition (wt% of the oxide)**									
Sample Name	Sample Location	Magma Type	SiO2	Al2O3	TiO2	MgO	FeO	MnO	CaO	Na2O	K2O	P2O5
GP107-04	GP107	B	75.6	14.0	0.17	0.15	1.27	0.06	0.96	3.24	4.59	0.01
WHA039D	WHA039	A	72.3	15.5	0.33	0.44	2.17	0.05	2.42	3.72	2.99	0.02
WHA039E	WHA039	A	71.7	16.6	0.36	0.51	2.41	0.06	2.14	3.42	2.80	0.02
WHA039F	WHA039	D	74.5	14.6	0.30	0.34	1.81	0.04	1.73	3.41	3.30	0.02
WHA039G	WHA039	A	73.2	15.3	0.34	0.44	2.24	0.05	2.17	3.51	2.82	0.02
WHA039H	WHA039	A	71.8	16.6	0.35	0.45	2.27	0.06	2.32	3.55	2.58	0.02
WHA039I	WHA039	A	73.1	14.9	0.32	0.44	2.14	0.06	2.16	3.44	3.44	0.02
WHA039J	WHA039	C	76.4	13.7	0.14	0.08	1.09	0.04	0.81	3.04	4.64	0.01
WHA039K	WHA039	A	72.3	16.2	0.35	0.45	2.28	0.06	2.21	3.46	2.67	0.02
WHA109C	WHA109	C	76.1	13.5	0.12	0.08	1.09	0.05	0.83	3.56	4.66	0.01
WHA109E	WHA109	B	76.3	13.4	0.14	0.11	1.16	0.05	0.90	3.53	4.42	0.01
WHA114A	WHA114	B	76.3	13.4	0.14	0.11	1.08	0.04	0.95	3.51	4.46	0.01
WHA114B	WHA114	B	76.3	13.4	0.14	0.11	1.10	0.04	0.96	3.52	4.43	0.01
WHAK415-A2	WHAK415	B	74.0	15.8	0.24	0.29	1.66	0.05	1.18	2.85	3.92	0.03
WHAK415-A3	WHAK415	B	74.8	15.0	0.17	0.15	1.29	0.04	1.01	2.90	4.59	0.03
WHAK415-A4	WHAK415	B	74.0	15.4	0.21	0.19	1.46	0.05	1.28	3.12	4.29	0.03

Sample Information	**Major-element whole-rock st dev (wt% of the oxide)**									
Sample Name	SiO2	Al2O3	TiO2	MgO	FeO	MnO	CaO	Na2O	K2O	P2O5
GP107-04	0.18	0.07	0.01	0.01	0.04	0.00	0.02	0.05	0.03	0.00
WHA039D	0.17	0.08	0.01	0.02	0.05	0.00	0.03	0.05	0.02	0.00
WHA039E	0.17	0.08	0.01	0.02	0.05	0.00	0.03	0.05	0.02	0.00
WHA039F	0.17	0.07	0.01	0.02	0.04	0.00	0.03	0.05	0.02	0.00
WHA039G	0.17	0.08	0.01	0.02	0.05	0.00	0.03	0.05	0.02	0.00
WHA039H	0.17	0.08	0.01	0.02	0.05	0.00	0.03	0.05	0.02	0.00
WHA039I	0.17	0.08	0.01	0.02	0.05	0.00	0.03	0.05	0.02	0.00
WHA039J	0.18	0.07	0.01	0.01	0.03	0.00	0.02	0.04	0.03	0.00
WHA039K	0.17	0.08	0.01	0.02	0.05	0.00	0.03	0.05	0.02	0.00
WHA109C	0.18	0.07	0.01	0.01	0.03	0.00	0.02	0.05	0.03	0.00
WHA109E	0.18	0.07	0.01	0.01	0.03	0.00	0.02	0.05	0.03	0.00
WHA114A	0.18	0.07	0.01	0.01	0.03	0.00	0.02	0.05	0.03	0.00
WHA114B	0.18	0.07	0.01	0.01	0.03	0.00	0.02	0.05	0.03	0.00
WHAK415-A2	0.17	0.08	0.01	0.02	0.04	0.00	0.02	0.04	0.03	0.00
WHAK415-A3	0.17	0.08	0.01	0.01	0.04	0.00	0.02	0.04	0.03	0.00
WHAK415-A4	0.17	0.08	0.01	0.01	0.04	0.00	0.02	0.04	0.03	0.00

Sample Information	**Trace-element whole-rock composition (ppm)**																			
Sample Name	Ni	Cr	V	Sc	Cu	Zn	Ga	Ba	Rb	Cs	Sr	Y	Zr	Hf	Nb	Ta	Mo	La	Ce	Nd
GP107-04	0.9	3.1	7.5	3.5	1.1	32	14	906	150	9.5	69	23	114	4.4	8.6	1.0	3.2	28	57	20
WHA039D	2.2	9.9	27	7.0	-	34	15	695	91	5.4	192	15	168	3.3	6.9	0.7	2.3	17	34	14
WHA039E	1.9	5.5	26	5.9	5.8	40	16	718	90	3.5	164	20	194	4.3	7.8	1.0	1.2	24	41	16
WHA039F	2.7	6.5	19	4.1	18	41	14	924	166	11	141	18	177	4.8	6.1	0.9	0.8	26	42	15
WHA039G	1.6	4.6	27	5.7	-	32	16	682	88	2.6	169	16	179	4.8	6.8	1.0	2.1	18	34	13
WHA039H	3.2	7.6	28	7.0	12	41	16	669	81	7.4	182	15	190	4.8	8.0	1.6	1.1	18	35	11
WHA039I	0.4	3.7	25	4.0	-	31	14	738	102	2.2	172	17	169	5.1	6.7	0.5	2.3	18	41	15
WHA039J	0.8	5.6	6.1	4.0	25	34	13	774	169	9.7	53	21	106	4.0	7.3	1.5	2.3	26	59	18
WHA039K	1.4	7.5	28	6.9	6.5	35	15	697	84	4.2	173	18	192	4.8	6.8	0.9	1.2	22	47	16
WHA109C	1.0	3.4	4.2	1.4	112	86	14	690	165	5.0	51	24	103	3.8	8.1	0.8	2.3	29	53	19
WHA109E	0.2	5.3	5.3	2.7	43	55	12	750	155	6.6	61	21	102	2.7	7.0	1.2	2.9	29	53	18
WHA114A	1.0	5.4	7.0	2.7	62	60	13	907	149	8.2	69	21	98	4.0	7.3	0.7	0.8	23	49	17
WHA114B	2.0	5.3	5.6	2.2	29	42	13	804	151	6.3	67	21	103	3.3	7.8	1.3	3.7	28	53	20
WHAK415-A2	0.2	1.7	14	4.2	0.7	26	14	1152	137	8.3	91	18	149	4.6	8.0	0.9	1.0	24	47	18
WHAK415-A3	2.5	4.0	8.4	3.8	13	23	14	825	157	7.2	72	22	126	3.3	7.5	0.9	1.0	25	52	19
WHAK415-A4	4.6	9.4	12	3.9	3.5	19	14	1256	154	8.8	107	18	140	3.3	7.7	1.2	1.6	26	49	18

Sample Name	Sm	Dy	Yb	Th	U	Tl	Pb	Sn	Bi
GP107-04	4.4	3.3	2.5	17	2.6	0.7	11	2.9	0.1
WHA039D	2.7	2.4	1.4	11	2.5	1.0	7.6	3.1	0.4
WHA039E	3.2	3.1	2.1	12	4.5	0.6	7.2	3.0	0.1
WHA039F	2.4	2.8	1.8	10	2.2	1.3	7.9	3.1	0.4
WHA039G	2.9	2.4	1.8	11	2.7	0.7	6.8	3.0	0.0
WHA039H	2.0	2.4	1.7	10	2.4	0.6	7.7	3.1	-
WHA039I	3.0	2.2	1.8	12	2.2	0.7	7.3	3.0	0.1
WHA039J	3.8	3.0	2.0	16	4.1	1.0	7.8	3.1	0.3
WHA039K	3.3	3.0	2.0	12	2.6	1.0	7.7	3.1	0.3
WHA109C	4.0	3.4	2.4	18	3.6	0.6	11	3.1	0.0
WHA109E	3.4	3.1	2.2	15	4.2	1.8	7.7	3.1	0.1
WHA114A	3.4	3.1	2.2	15	3.1	1.1	9.3	3.1	0.4
WHA114B	3.7	3.1	2.1	15	3.0	1.0	9.9	3.1	0.2
WHAK415-A2	3.6	2.8	1.7	17	3.5	0.4	4.3	2.7	0.1
WHAK415-A3	3.6	3.3	2.1	18	2.6	1.1	3.3	3.1	0.3
WHAK415-A4	3.3	2.7	1.9	15	2.9	1.4	0.8	3.1	0.2

Sample Name	Ni	Cr	V	Sc	Cu	Zn	Ga	Ba	Rb	Cs	Sr	Y	Zr	Hf	Nb	Ta	Mo	La	Ce	Nd
GP107-04	bdl	2.17	1.47	0.70	bdl	1.77	0.80	12.0	2.16	1.74	2.46	1.30	4.54	0.54	0.81	bdl	0.91	2.25	3.76	1.71
WHA039D	1.50	2.50	2.19	0.75	bdl	1.81	0.81	10.6	1.75	1.67	4.30	1.09	5.28	0.51	0.79	bdl	0.81	2.13	3.60	1.69
WHA039E	1.48	2.31	2.16	0.74	1.53	1.99	0.83	10.8	1.75	1.63	3.94	1.23	5.59	0.53	0.80	bdl	0.66	2.21	3.65	1.70
WHA039F	1.53	2.36	1.95	0.71	2.06	2.01	0.80	12.1	2.26	1.76	3.62	1.16	5.39	0.55	0.77	bdl	0.59	2.23	3.66	1.69
WHA039G	1.45	2.26	2.20	0.73	bdl	1.78	0.82	10.5	1.73	1.60	4.01	1.12	5.41	0.55	0.79	bdl	0.78	2.14	3.59	1.69
WHA039H	1.57	2.41	2.22	0.75	1.85	2.01	0.82	10.5	1.68	1.70	4.17	1.10	5.54	0.55	0.80	1.14	0.64	2.14	3.61	1.68
WHA039I	bdl	2.21	2.13	0.71	bdl	1.74	0.81	10.9	1.83	1.59	4.04	1.14	5.29	0.55	0.78	bdl	0.81	2.14	3.65	1.69
WHA039J	bdl	2.32	1.39	0.71	2.25	1.82	0.79	11.2	2.28	1.74	2.16	1.25	4.40	0.53	0.79	1.14	0.81	2.23	3.78	1.70
WHA039K	bdl	2.41	2.21	0.75	1.57	1.85	0.82	10.7	1.70	1.64	4.05	1.18	5.57	0.55	0.79	bdl	0.66	2.19	3.70	1.70
WHA109C	bdl	2.19	1.26	0.65	3.36	3.05	0.80	10.6	2.25	1.66	2.11	1.32	4.36	0.52	0.81	bdl	0.81	2.26	3.74	1.71
WHA109E	bdl	2.31	1.33	0.68	2.59	2.35	0.78	11.0	2.19	1.69	2.31	1.26	4.34	0.49	0.79	1.13	0.89	2.26	3.74	1.70
WHA114A	bdl	2.31	1.44	0.68	2.87	2.47	0.79	12.0	2.15	1.72	2.46	1.26	4.27	0.53	0.79	bdl	0.59	2.20	3.71	1.70
WHA114B	1.49	2.31	1.35	0.67	2.34	2.04	0.79	11.4	2.17	1.69	2.42	1.26	4.37	0.51	0.80	1.13	0.98	2.25	3.74	1.71
WHAK415-A2	bdl	bdl	1.77	0.71	bdl	1.59	0.80	13.4	2.08	1.72	2.85	1.17	5.03	0.54	0.81	bdl	0.62	2.21	3.70	1.70
WHAK415-A3	1.52	2.23	1.51	0.70	1.87	1.51	0.80	11.5	2.20	1.70	2.51	1.28	4.71	0.51	0.80	bdl	0.62	2.22	3.73	1.70
WHAK415-A4	1.63	2.48	1.70	0.71	1.36	1.36	0.80	13.9	2.19	1.72	3.11	1.18	4.92	0.51	0.80	1.13	0.72	2.23	3.71	1.70

Sample Name	Sm	Dy	Yb	Th	U	Tl	Pb	Sn	Bi
GP107-04	0.384	0.309	0.664	1.19	1.131	bdl	1.716	2.507	bdl
WHA039D	0.374	0.286	0.662	1.144	1.129	bdl	1.558	2.519	bdl
WHA039E	0.377	0.303	0.663	1.15	1.168	bdl	1.537	2.516	bdl
WHA039F	0.372	0.295	0.663	1.141	1.12	bdl	1.574	2.523	bdl
WHA039G	0.375	0.285	0.663	1.148	1.133	bdl	1.521	2.516	bdl
WHA039H	0.368	0.286	0.663	1.141	1.125	bdl	1.564	2.52	bdl
WHA039I	0.376	0.278	0.663	1.153	1.121	bdl	1.543	2.513	bdl
WHA039J	0.381	0.3	0.663	1.182	1.161	bdl	1.569	2.521	bdl
WHA039K	0.378	0.3	0.663	1.157	1.131	bdl	1.564	2.52	bdl
WHA109C	0.382	0.311	0.664	1.193	1.152	bdl	1.72	2.52	bdl
WHA109E	0.378	0.305	0.663	1.178	1.164	1.601	1.564	2.524	bdl
WHA114A	0.378	0.305	0.663	1.178	1.143	bdl	1.638	2.525	bdl
WHA114B	0.38	0.305	0.663	1.177	1.14	bdl	1.666	2.523	bdl
WHAK415-A2	0.38	0.297	0.663	1.19	1.151	bdl	1.378	2.499	bdl
WHAK415-A3	0.379	0.309	0.663	1.194	1.131	bdl	1.318	2.523	bdl
WHAK415-A4	0.378	0.293	0.663	1.175	1.138	bdl	bdl	2.524	bdl

Sample Information	Extraction pressures (MPa)											
Sample Name	qtz-1feld	feld-opx (ΔNNO)	qtz-1feld-opx (ΔNNO)	feld-opx (ΔNNO+0.5)	qtz-1feld-opx (ΔNNO+0.5)	feld-opx (ΔNNO+1)	qtz-1feld-opx (ΔNNO+1)	feld-opx (ΔNNO+1.5)	qtz-1feld-opx (ΔNNO+1.5)	feld-opx (ΔNNO+2)	qtz-1feld-opx (ΔNNO+2)
GP107-04	249	309	-	397	-	323	-	-	-	-	-
WHA039D	-	220	-	268	-	-	-	-	-	-	-
WHA039E	438	178	-	230	-	292	-	358	-	-	-
WHA039F	349	192	-	248	-	318	316	-	347	-	-
WHA039G	393	189	-	242	-	-	-	-	-	-	-
WHA039H	463	233	-	289	-	356	-	-	-	-	-
WHA039I	393	171	-	221	-	-	-	-	-	-	-
WHA039J	153	-	-	364	-	-	-	-	-	-	-
WHA039K	-	215	-	270	-	333	-	-	-	-	-
WHA109C	242	331	-	328	-	308	-	-	-	-	-
WHA109E	220	369	-	411	-	298	-	147	-	-	-
WHA114A	226	366	-	381	-	298	-	-	-	-	-
WHA114B	229	364	-	391	-	298	-	-	-	-	-
WHAK415-A2	315	187	-	248	-	324	-	-	-	-	-
WHAK415-A3	276	313	-	407	-	-	-	-	-	-	-
WHAK415-A4	355	308	-	369	-	-	-	-	-	-	-

Table 4

Sample Information			Major Element Mean (outliers excluded) (wt% of the oxide)								
Sample Name	Sample Location	Magma Type	SiO2	Al2O3	TiO2	MgO	FeO	MnO	CaO	Na2O	K2O
WHA039D	WHA039	A	77.8	12.6	0.17	0.04	0.39	0.01	0.70	3.33	4.95
GP115a-06	GP115a	B	77.8	12.7	0.09	0.01	0.39	0.04	0.55	3.53	4.98
GP115a-09	GP115a	A	77.9	12.5	0.19	0.07	0.57	0.02	0.75	3.40	4.67
GP115a-12	GP115a	A	77.6	12.6	0.18	0.09	0.66	0.04	0.77	3.39	4.72
GP115c-14	GP115c	A	77.8	12.5	0.19	0.05	0.37	0.03	0.75	2.92	5.35
GP115c-18	GP115c	A	77.6	12.6	0.18	0.08	0.70	0.04	0.79	3.34	4.68
GP115c-20	GP115c	A	77.7	12.6	0.16	0.04	0.38	0.03	0.74	3.22	5.11
WHA039A	WHA039	A	77.8	12.6	0.17	0.03	0.38	0.04	0.69	3.28	5.01
WHA039B	WHA039	A	77.8	12.7	0.18	0.02	0.38	0.02	0.72	3.42	4.81
WHA039C	WHA039	A	78.0	12.6	0.18	0.02	0.39	0.02	0.82	3.25	4.77
GP107-04	GP107	B	77.5	12.6	0.08	0.05	0.71	0.05	0.61	3.59	4.82
WHA039E	WHA039	A	78.0	12.5	0.22	0.05	0.42	0.01	0.85	2.75	5.17
WHA039F	WHA039	D	78.0	12.6	0.13	0.06	0.37	0.04	0.82	3.03	4.94
WHA039G	WHA039	A	77.8	12.6	0.19	0.03	0.40	0.01	0.71	3.33	4.90
WHA039H	WHA039	A	77.9	12.7	0.16	0.04	0.31	0.02	0.73	3.13	4.98
WHA039I	WHA039	A	77.9	12.7	0.18	0.03	0.28	0.05	0.70	2.52	5.59
WHA039J	WHA039	C	77.7	12.7	0.08	0.03	0.35	0.04	0.55	3.44	5.06
WHA039K	WHA039	A	78.0	12.5	0.16	0.04	0.36	0.03	0.84	2.80	5.24
WHA109A	WHA109	A	77.8	12.5	0.17	0.08	0.95	0.04	0.72	3.17	4.61
WHA109B	WHA109	C	77.8	12.5	0.08	0.04	0.70	0.06	0.49	3.37	4.98
WHA109C	WHA109	C	77.6	12.6	0.06	0.05	0.65	0.04	0.59	3.02	5.42
WHA109D	WHA109	C	77.5	12.6	0.06	0.03	0.72	0.06	0.50	3.25	5.29
WHA109E	WHA109	B	77.6	12.6	0.06	0.04	0.69	0.06	0.53	3.12	5.25
WHA114A	WHA114	B	77.6	12.6	0.07	0.04	0.69	0.06	0.58	3.58	4.88
WHA114B	WHA114	B	77.6	12.6	0.09	0.04	0.61	0.03	0.59	3.61	4.88
WHA114C	WHA114	B	77.6	12.6	0.07	0.04	0.55	0.05	0.59	3.55	4.90
WHA114D	WHA114	B	77.6	12.6	0.10	0.04	0.60	0.03	0.60	3.55	4.84
WHAK415-A1	WHAK415	B	77.7	12.6	0.09	0.04	0.34	0.04	0.59	2.93	5.65
WHAK415-A3	WHAK415	B	77.6	12.6	0.08	0.02	0.34	0.03	0.57	3.04	5.71
WHAK415-A4	WHAK415	B	77.6	12.6	0.11	0.02	0.31	0.03	0.61	2.99	5.74
WHAK415-A5	WHAK415	A	77.7	12.6	0.12	0.05	0.38	0.05	0.74	2.75	5.61
WHAK415-A6	WHAK415	B	77.7	12.6	0.10	0.04	0.34	0.02	0.63	2.72	5.78
WHAK415-A7	WHAK415	B	77.6	12.6	0.08	0.02	0.39	0.04	0.58	2.79	5.90
WHAK415-A8	WHAK415	B	77.7	12.6	0.06	0.02	0.37	0.02	0.60	2.88	5.76
WHAK602	WHAK602	Unclassified	77.6	12.5	0.17	0.01	0.21	0.03	0.34	2.46	6.75
WHAK602A	WHAK602	Unclassified	77.5	12.5	0.19	0.01	0.25	-	0.39	2.39	6.76
WHAK602C	WHAK602	Unclassified	77.5	12.4	0.16	0.03	0.47	0.01	0.25	2.63	6.56
WHAK602E	WHAK602	Unclassified	77.2	12.4	0.13	0.06	0.68	0.00	0.24	2.88	6.37

Sample Information	**Major Element St Dev (wt% of the oxide)**								
Sample Name	SiO2	Al2O3	TiO2	MgO	FeO	MnO	CaO	Na2O	K2O
WHA039D	0.11	0.08	0.03	0.03	0.08	0.01	0.04	0.08	0.13
GP115a-06	0.09	0.09	0.03	0.01	0.09	0.04	0.05	0.15	0.17
GP115a-09	0.20	0.05	0.04	0.04	0.21	0.03	0.05	0.08	0.13
GP115a-12	0.07	0.07	0.04	0.03	0.14	0.04	0.05	0.07	0.11
GP115c-14	0.13	0.07	0.04	0.03	0.08	0.03	0.03	0.23	0.31
GP115c-18	0.12	0.06	0.04	0.03	0.11	0.04	0.04	0.05	0.06
GP115c-20	0.07	0.05	0.05	0.02	0.13	0.03	0.04	0.14	0.26
WHA039A	0.13	0.05	0.01	0.03	0.07	0.03	0.04	0.10	0.10
WHA039B	0.14	0.08	0.04	0.02	0.06	0.02	0.03	0.07	0.08
WHA039C	0.23	0.16	0.07	0.02	0.12	0.03	0.06	0.09	0.10
GP107-04	0.10	0.04	0.05	0.03	0.06	0.04	0.03	0.04	0.05
WHA039E	0.31	0.22	0.05	0.04	0.10	0.01	0.07	0.44	0.30
WHA039F	0.37	0.19	0.05	0.03	0.10	0.04	0.07	0.46	0.40
WHA039G	0.13	0.05	0.04	0.03	0.08	0.02	0.04	0.07	0.10
WHA039H	0.15	0.05	0.06	0.03	0.05	0.02	0.03	0.17	0.09
WHA039I	0.13	0.13	0.04	0.02	0.08	0.04	0.03	0.18	0.15
WHA039J	0.11	0.08	0.05	0.02	0.05	0.04	0.04	0.10	0.11
WHA039K	0.21	0.25	0.07	0.02	0.08	0.03	0.09	0.41	0.34
WHA109A	0.20	0.11	0.04	0.03	0.08	0.04	0.06	0.14	0.07
WHA109B	0.08	0.04	0.06	0.03	0.07	0.04	0.04	0.11	0.07
WHA109C	0.31	0.22	0.05	0.02	0.19	0.03	0.07	0.55	0.52
WHA109D	0.13	0.09	0.04	0.02	0.05	0.04	0.04	0.12	0.14
WHA109E	0.33	0.11	0.04	0.02	0.20	0.05	0.03	0.47	0.36
WHA114A	0.12	0.08	0.03	0.03	0.07	0.04	0.04	0.06	0.04
WHA114B	0.10	0.07	0.06	0.03	0.14	0.03	0.04	0.04	0.08
WHA114C	0.09	0.03	0.04	0.03	0.09	0.05	0.04	0.05	0.07
WHA114D	0.11	0.10	0.05	0.02	0.07	0.04	0.03	0.05	0.06
WHAK415-A1	0.11	0.05	0.02	0.03	0.07	0.03	0.03	0.03	0.07
WHAK415-A3	0.10	0.04	0.05	0.02	0.06	0.03	0.03	0.06	0.07
WHAK415-A4	0.08	0.07	0.05	0.02	0.04	0.03	0.04	0.05	0.09
WHAK415-A5	0.11	0.08	0.05	0.02	0.07	0.05	0.03	0.05	0.07
WHAK415-A6	0.11	0.06	0.05	0.04	0.08	0.02	0.03	0.05	0.06
WHAK415-A7	0.08	0.04	0.04	0.02	0.06	0.04	0.04	0.04	0.04
WHAK415-A8	0.10	0.03	0.04	0.02	0.05	0.02	0.03	0.04	0.05
WHAK602	0.16	0.05	0.03	0.01	0.05	0.03	0.05	0.14	0.06
WHAK602A	0.17	0.06	0.04	0.02	0.07	-	0.04	0.13	0.05
WHAK602C	0.19	0.04	0.05	0.03	0.15	0.02	0.02	0.06	0.07
WHAK602E	0.13	0.12	0.02	0.06	0.15	0.01	0.08	0.12	0.12

Sample Information	**Trace Element Mean (outliers excluded) (ppm)**												
Sample Name	Li	Al	Si	Sc	V	Fe	Ni	Zn	Ga	Rb	Sr	Y	Zr
WHA039D	43	64149	363574	9.6	2.7	39	0.3	15	67	154	46	18	114
GP115a-06	55	61479	363528	15	0.4	37	0.6	27	39	193	18	20	62
GP115a-09	42	61509	363761	9.5	2.8	45	0.0	22	70	164	46	17	106
GP115a-12	45	61073	362639	11	2.8	47	0.5	21	67	158	43	17	109
GP115c-14	23	67191	363902	10	3.0	58	0.8	11	73	160	45	18	120
GP115c-18	40	62348	362593	9.6	2.6	52	0.2	22	70	172	48	19	112
GP115c-20	39	61546	363434	11	2.9	43	0.3	17	69	161	47	19	110
WHA039A	36	68776	363200	14	2.9	34	0.1	9.5	89	175	45	18	120
WHA039B	39	113900	363200	15	4.0	85	0.6	19	103	149	40	27	155
WHA039C	31	97773	363200	14	3.0	97	0.4	23	103	150	48	19	164
GP107-04	49	62862	362266	10.0	0.4	50	0.4	23	34	174	20	20	62
WHA039E	32	111688	363060	20	3.8	136	1.9	27	90	143	35	29	202
WHA039F	49	62004	363574	14	1.0	45	0.4	29	90	165	48	14	76
WHA039G	41	66575	363528	15	2.6	42	0.2	12	85	166	43	17	106
WHA039H	29	72738	363761	17	3.0	37	0.5	7.5	85	162	42	17	123
WHA039I	25	70116	362920	16	3.0	87	1.3	9.8	89	181	46	18	124
WHA039J	41	69986	363247	15	0.5	39	0.5	15	34	194	14	23	68
WHA039K	-	-	-	-	-	-	-	-	-	-	-	-	-
WHA109A	20	66955	362266	14	2.5	51	0.2	18	91	176	50	18	111
WHA109B	26	65292	362266	13	0.3	43	0.1	16	31	196	13	22	64
WHA109C	18	56255	361985	14	0.4	38	0.2	20	27	188	11	18	52
WHA109D	36	64139	362265	14	0.4	49	0.2	28	31	203	13	21	63
WHA109E	52	62681	362125	15	0.5	53	0.3	30	44	188	19	20	61
WHA114A	52	62203	362686	9.2	0.5	50	0.4	24	37	179	20	20	64
WHA114B	52	62560	362593	14	0.5	41	0.3	21	45	182	19	20	63
WHA114C	44	64277	362733	13	0.6	36	0.1	16	42	183	18	20	63
WHA114D	48	64513	362733	14	0.4	36	0.1	16	44	185	18	21	67
WHAK415-A1	-	-	-	-	-	-	-	-	-	-	-	-	-
WHAK415-A3	-	-	-	-	-	-	-	-	-	-	-	-	-
WHAK415-A4	-	-	-	-	-	-	-	-	-	-	-	-	-
WHAK415-A5	35	82018	363154	16	1.5	37	0.8	7.7	101	208	47	17	106
WHAK415-A6	44	79001	363200	15	0.6	31	0.5	6.2	79	246	30	18	85
WHAK415-A7	47	64176	362733	15	0.5	34	0.5	12	42	239	20	22	66
WHAK415-A8	40	68052	362967	14	0.6	28	0.1	7.0	40	247	19	22	73
WHAK602	-	-	-	-	-	-	-	-	-	-	-	-	-
WHAK602A	32	67629	362078	19	2.6	27	0.1	7.4	79	502	14	18	115
WHAK602C	83	63220	361985	17	3.4	53	0.7	12	44	781	7.0	18	109
WHAK602E	135	67065	360957	16	2.9	30	0.1	7.2	35	972	5.5	18	108

Sample Information	**Trace Element Mean (outliers excluded) (ppm)**												
Sample Name	Nb	Cs	Ba	La	Ce	Pr	Nd	Sm	Eu	Tb	Gd	Dy	Ho
WHA039D	7.7	6.7	795	23	45	4.6	17	3.2	0.3	0.5	2.7	2.8	0.6
GP115a-06	7.9	8.9	319	26	53	5.0	18	3.7	0.2	0.5	3.0	3.3	0.6
GP115a-09	7.5	7.4	836	22	43	4.3	16	3.2	0.3	0.4	2.5	2.9	0.6
GP115a-12	6.9	7.0	770	22	42	4.2	15	3.2	0.3	0.4	2.7	2.8	0.6
GP115c-14	7.0	7.5	817	25	41	4.7	17	2.6	0.3	0.4	3.0	3.1	0.6
GP115c-18	7.1	7.5	832	25	44	4.5	16	3.3	0.4	0.5	2.7	2.8	0.6
GP115c-20	7.5	7.3	884	25	40	4.5	18	3.2	0.4	0.5	2.9	3.0	0.6
WHA039A	7.1	7.8	829	24	44	4.5	17	3.1	0.3	0.5	2.7	2.9	0.6
WHA039B	11	8.0	910	36	48	6.4	22	4.2	0.5	0.7	4.0	4.3	0.9
WHA039C	9.1	7.4	887	29	39	4.8	16	3.1	0.4	0.5	2.7	3.0	0.7
GP107-04	7.5	8.7	351	27	52	4.9	19	3.5	0.2	0.5	2.9	3.3	0.7
WHA039E	12	9.1	824	35	45	6.7	25	4.6	0.7	0.8	4.8	4.4	1.0
WHA039F	6.3	6.6	926	21	42	3.9	14	2.7	0.4	0.4	2.3	2.3	0.5
WHA039G	6.8	7.5	808	22	42	4.3	16	3.2	0.4	0.5	2.8	2.7	0.6
WHA039H	6.6	7.4	783	22	42	3.9	17	3.2	0.4	0.4	2.7	2.9	0.6
WHA039I	7.8	8.2	850	24	44	4.0	17	3.1	0.3	0.5	3.0	3.0	0.6
WHA039J	8.9	10	215	26	54	5.2	19	3.6	0.2	0.6	3.3	3.7	0.8
WHA039K	-	-	-	-	-	-	-	-	-	-	-	-	-
WHA109A	6.4	7.4	868	25	45	4.5	17	3.1	0.2	0.5	2.8	2.9	0.6
WHA109B	7.8	9.3	211	26	52	5.2	18	3.8	0.1	0.6	3.2	3.6	0.8
WHA109C	8.0	8.6	181	22	49	4.4	17	4.0	0.2	0.6	3.0	3.1	0.6
WHA109D	8.1	9.5	209	26	54	5.1	19	3.5	0.1	0.5	3.1	3.5	0.8
WHA109E	7.4	8.4	342	25	52	4.9	18	3.1	0.2	0.5	3.1	3.0	0.7
WHA114A	7.7	8.8	346	27	53	5.2	20	3.7	0.2	0.5	2.8	3.3	0.7
WHA114B	7.7	8.8	333	27	54	5.2	18	3.6	0.2	0.5	2.9	3.1	0.7
WHA114C	7.5	8.5	311	26	53	4.9	18	3.5	0.2	0.5	3.0	3.2	0.7
WHA114D	8.0	8.7	327	29	55	5.4	19	3.7	0.2	0.5	3.2	3.4	0.7
WHAK415-A1	-	-	-	-	-	-	-	-	-	-	-	-	-
WHAK415-A3	-	-	-	-	-	-	-	-	-	-	-	-	-
WHAK415-A4	-	-	-	-	-	-	-	-	-	-	-	-	-
WHAK415-A5	7.4	11	887	25	46	4.9	19	3.6	0.4	0.5	2.8	2.8	0.6
WHAK415-A6	8.0	14	678	27	55	5.0	19	3.1	0.3	0.5	2.7	3.1	0.7
WHAK415-A7	8.1	9.7	344	29	57	5.6	19	3.7	0.2	0.6	3.2	3.5	0.7
WHAK415-A8	8.7	12	308	30	58	5.7	20	3.9	0.2	0.6	3.3	3.7	0.8
WHAK602	-	-	-	-	-	-	-	-	-	-	-	-	-
WHAK602A	6.8	42	710	23	41	4.3	16	3.1	0.2	0.5	2.8	2.9	0.6
WHAK602C	7.1	75	348	22	46	4.3	15	3.2	0.1	0.5	2.6	2.9	0.6
WHAK602E	7.2	93	238	24	46	4.7	17	3.1	0.0	0.4	2.7	3.1	0.7

Sample Information	**Trace Element Mean (outliers excluded) (ppm)**								
Sample Name	Er	Tm	Yb	Lu	Hf	Ta	Pb	Th	U
WHA039D	1.8	0.3	2.3	0.3	3.4	0.6	11	14	3.5
GP115a-06	1.9	0.3	2.5	0.4	2.5	0.7	12	17	4.6
GP115a-09	1.8	0.3	2.2	0.3	3.1	0.6	13	14	3.7
GP115a-12	1.8	0.3	2.2	0.3	3.2	0.6	13	15	3.6
GP115c-14	1.9	0.3	2.2	0.3	3.4	0.7	13	15	3.5
GP115c-18	1.8	0.3	2.2	0.3	3.2	0.6	17	15	3.6
GP115c-20	1.9	0.3	2.2	0.3	3.1	0.6	13	14	3.4
WHA039A	1.9	0.3	2.2	0.3	3.7	0.7	11	15	3.7
WHA039B	2.7	0.4	3.0	0.4	4.8	0.8	15	22	4.1
WHA039C	1.9	0.3	2.1	0.3	4.8	0.9	14	17	3.4
GP107-04	2.1	0.3	2.4	0.4	2.5	0.7	11	16	4.0
WHA039E	2.6	0.4	3.1	0.4	5.8	1.1	14	23	4.3
WHA039F	1.5	0.2	1.9	0.3	2.6	0.5	15	12	3.2
WHA039G	1.7	0.3	2.1	0.3	3.1	0.6	10	14	3.6
WHA039H	1.6	0.3	2.1	0.3	3.7	0.6	11	15	2.9
WHA039I	1.8	0.3	2.2	0.4	3.9	0.7	13	15	3.2
WHA039J	2.4	0.4	2.8	0.4	2.8	0.9	13	18	4.9
WHA039K	-	-	-	-	-	-	-	-	-
WHA109A	1.9	0.3	2.3	0.3	3.4	0.6	12	15	3.5
WHA109B	2.2	0.4	2.7	0.4	2.6	0.8	9.4	17	4.5
WHA109C	2.0	0.3	2.4	0.4	2.1	0.8	11	15	4.5
WHA109D	2.3	0.4	2.7	0.4	2.6	0.8	10	17	4.9
WHA109E	1.9	0.3	2.3	0.3	2.4	0.8	12	16	4.2
WHA114A	2.1	0.3	2.5	0.4	2.3	0.7	11	16	4.3
WHA114B	2.0	0.3	2.5	0.3	2.4	0.7	11	16	4.3
WHA114C	2.0	0.3	2.5	0.4	2.5	0.8	13	16	4.2
WHA114D	2.1	0.3	2.6	0.4	2.6	0.8	12	17	4.3
WHAK415-A1	-	-	-	-	-	-	-	-	-
WHAK415-A3	-	-	-	-	-	-	-	-	-
WHAK415-A4	-	-	-	-	-	-	-	-	-
WHAK415-A5	1.6	0.3	2.1	0.3	3.4	0.7	3.8	16	3.7
WHAK415-A6	1.9	0.3	2.4	0.4	3.0	0.8	3.7	17	4.1
WHAK415-A7	2.2	0.4	2.8	0.4	2.7	0.8	3.5	18	4.8
WHAK415-A8	2.2	0.4	2.6	0.4	2.7	0.9	3.2	18	4.7
WHAK602	-	-	-	-	-	-	-	-	-
WHAK602A	2.0	0.3	2.2	0.4	3.7	0.6	5.1	14	4.1
WHAK602C	1.9	0.3	2.2	0.4	3.2	0.6	5.4	14	3.5
WHAK602E	1.8	0.3	2.1	0.3	3.2	0.6	6.3	14	3.6

Sample Information	**Trace Element St Dev (ppm)**												
Sample Name	Li	Al	Si	Sc	V	Fe	Ni	Zn	Ga	Rb	Sr	Y	Zr
WHA039D	5.7	4395	0.0	1.1	0.4	11.7	0.6	7.3	3.2	9.5	1.8	1.4	6.3
GP115a-06	2.0	3584	0.0	1.1	0.0	6.2	0.2	3.2	2.2	15.6	1.0	0.8	2.7
GP115a-09	3.0	3772	0.0	1.4	0.3	10.7	0.4	9.0	2.8	11.7	2.9	0.6	5.5
GP115a-12	8.7	3268	0.0	0.3	0.2	11.5	0.4	5.8	2.6	14.7	3.1	0.7	4.9
GP115c-14	7.2	8288	0.0	1.2	0.3	34.7	0.2	2.3	4.0	8.5	3.9	1.5	12.3
GP115c-18	3.2	976	0.0	0.6	0.4	7.6	0.3	7.0	3.4	11.4	1.4	0.9	5.4
GP115c-20	11.8	2596	0.0	1.9	0.2	15.3	0.5	5.3	3.5	8.6	2.5	1.7	8.8
WHA039A	5.3	4103	0.0	0.8	0.2	13.7	0.1	2.3	6.0	12.2	1.5	0.3	10.6
WHA039B	3.7	33718	0.0	1.2	0.8	17.6	0.3	5.0	10.3	27.4	2.6	6.1	24.9
WHA039C	2.5	20328	0.0	1.3	0.5	36.0	0.3	7.5	5.8	12.0	6.1	1.9	26.1
GP107-04	2.5	2394	0.0	0.9	0.1	8.1	0.3	5.4	0.7	8.8	1.3	0.6	1.3
WHA039E	4.3	29914	0.0	1.7	0.9	75.5	1.5	9.2	13.9	36.2	2.4	4.7	33.0
WHA039F	2.2	4320	0.0	0.3	0.1	4.9	0.1	3.4	5.2	6.3	2.0	1.0	4.2
WHA039G	4.9	6198	0.0	1.1	0.2	10.1	0.1	0.9	5.2	9.5	1.5	1.0	8.3
WHA039H	7.7	12063	0.0	0.3	0.2	11.7	0.0	6.0	3.5	6.5	1.4	3.8	6.6
WHA039I	3.7	5921	0.0	1.5	0.4	43.4	0.4	4.5	5.8	29.0	3.5	2.4	10.2
WHA039J	3.7	4407	0.0	1.5	0.2	10.6	0.2	1.9	3.9	4.1	1.0	1.7	3.5
WHA039K	-	-	-	-	-	-	-	-	-	-	-	-	-
WHA109A	5.3	2254	0.0	0.9	0.3	9.0	0.2	3.2	4.3	6.8	3.6	1.3	5.2
WHA109B	3.0	3256	0.0	0.5	0.0	5.1	0.1	4.3	0.7	7.2	0.4	1.2	3.1
WHA109C	0.5	3081	0.0	1.7	0.1	4.9	0.0	1.3	0.8	2.5	1.4	0.6	3.0
WHA109D	7.3	2769	0.0	0.7	0.1	7.2	0.2	3.9	1.6	7.0	0.4	0.7	2.7
WHA109E	9.8	721	0.0	1.2	0.1	2.3	0.1	0.1	0.5	4.2	1.4	0.9	0.4
WHA114A	2.4	3279	0.0	1.4	0.0	1.1	0.3	4.9	1.3	10.6	1.1	0.6	2.8
WHA114B	2.3	5620	0.0	1.2	0.1	7.6	0.6	7.8	2.0	8.2	1.6	1.6	6.4
WHA114C	5.7	5253	0.0	0.7	0.2	9.5	0.1	2.8	3.1	10.0	1.0	1.9	7.4
WHA114D	2.9	7141	0.0	0.6	0.0	8.9	0.1	6.7	5.1	13.4	1.3	2.5	8.5
WHAK415-A1	-	-	-	-	-	-	-	-	-	-	-	-	-
WHAK415-A3	-	-	-	-	-	-	-	-	-	-	-	-	-
WHAK415-A4	-	-	-	-	-	-	-	-	-	-	-	-	-
WHAK415-A5	2.2	1653	0.0	0.2	0.2	8.6	0.6	0.1	0.2	3.6	1.3	1.1	0.6
WHAK415-A6	2.3	10693	0.0	0.7	0.1	5.1	0.2	2.0	5.8	10.6	0.7	1.6	11.0
WHAK415-A7	9.8	5034	0.0	1.1	0.1	4.6	0.0	7.9	10.2	12.9	2.2	2.5	9.5
WHAK415-A8	5.3	7358	0.0	0.7	0.2	4.4	0.1	2.2	4.7	13.7	1.1	1.6	10.9
WHAK602	-	-	-	-	-	-	-	-	-	-	-	-	-
WHAK602A	9.4	1708	0.0	0.7	0.3	8.8	0.2	2.0	6.0	28.0	1.9	0.9	3.2
WHAK602C	28.7	2006	0.0	1.5	0.6	24.1	0.6	3.2	7.6	50.2	2.6	1.7	10.5
WHAK602E	51.5	3417	0.0	0.2	0.1	14.4	0.1	2.7	7.6	27.1	2.4	0.2	7.5

Sample Information	**Trace Element St Dev (ppm)**												
Sample Name	Nb	Cs	Ba	La	Ce	Pr	Nd	Sm	Eu	Tb	Gd	Dy	Ho
WHA039D	0.7	0.6	67	1.5	3.2	0.7	1.7	0.5	0.1	0.1	0.3	0.5	0.0
GP115a-06	0.7	0.3	18	2.3	2.9	0.5	0.9	0.2	0.0	0.0	0.3	0.3	0.0
GP115a-09	0.4	0.4	64	0.6	1.2	0.5	1.5	0.4	0.0	0.0	0.2	0.2	0.1
GP115a-12	0.6	0.5	58	1.5	3.1	0.2	0.9	0.6	0.0	0.0	0.2	0.3	0.1
GP115c-14	1.5	0.6	45	3.2	2.6	0.2	3.3	0.6	0.0	0.0	0.2	0.2	0.1
GP115c-18	0.5	0.2	26	1.0	1.7	0.3	1.4	0.7	0.0	0.0	0.2	0.2	0.1
GP115c-20	1.0	0.5	29	1.0	3.6	0.2	2.2	0.6	0.1	0.1	0.3	0.2	0.0
WHA039A	0.4	0.5	46	0.9	3.4	0.3	0.8	0.4	0.0	0.0	0.3	0.2	0.0
WHA039B	2.4	0.6	54	6.9	6.4	1.3	3.8	0.8	0.2	0.2	1.0	1.0	0.2
WHA039C	1.9	0.5	84	3.6	5.1	0.5	1.8	0.5	0.0	0.1	0.2	0.3	0.1
GP107-04	0.2	0.4	20	0.7	3.3	0.3	1.4	0.3	0.0	0.0	0.2	0.2	0.1
WHA039E	3.6	1.6	138	7.8	8.5	1.0	6.1	1.0	0.0	0.1	0.7	1.0	0.0
WHA039F	0.4	0.4	56	1.8	2.0	0.1	0.3	0.2	0.0	0.0	0.2	0.2	0.1
WHA039G	0.7	0.5	12	1.8	2.1	0.2	1.4	0.5	0.0	0.0	0.2	0.2	0.0
WHA039H	1.8	0.1	22	4.8	0.8	1.0	0.6	0.0	0.0	0.1	0.4	0.2	0.0
WHA039I	0.9	1.2	64	2.1	6.6	0.2	1.4	0.8	0.0	0.0	0.3	0.2	0.0
WHA039J	0.5	0.6	24	1.6	2.9	0.5	0.7	0.2	0.0	0.0	0.1	0.2	0.0
WHA039K	-	-	-	-	-	-	-	-	-	-	-	-	-
WHA109A	0.4	0.2	44	1.8	1.5	0.5	1.3	0.4	0.0	0.0	0.3	0.3	0.0
WHA109B	0.5	0.4	9	1.3	2.4	0.3	1.0	0.3	0.0	0.0	0.2	0.2	0.0
WHA109C	0.7	0.4	3	2.4	2.3	0.1	1.4	0.4	0.0	0.0	0.2	0.3	0.0
WHA109D	0.3	0.4	13	0.9	2.0	0.2	0.9	0.3	0.0	0.0	0.2	0.1	0.0
WHA109E	0.1	0.5	11	0.4	3.4	0.1	0.3	0.2	0.0	0.0	0.1	0.0	0.0
WHA114A	0.3	0.3	11	0.5	2.1	0.2	1.5	0.6	0.0	0.0	0.3	0.1	0.1
WHA114B	0.6	0.5	18	2.4	2.9	0.3	1.5	0.4	0.0	0.1	0.2	0.2	0.1
WHA114C	0.7	0.3	20	2.0	2.3	0.4	1.3	0.4	0.0	0.0	0.3	0.3	0.1
WHA114D	0.9	0.5	33	3.7	2.9	0.5	2.3	0.6	0.0	0.1	0.4	0.4	0.1
WHAK415-A1	-	-	-	-	-	-	-	-	-	-	-	-	-
WHAK415-A3	-	-	-	-	-	-	-	-	-	-	-	-	-
WHAK415-A4	-	-	-	-	-	-	-	-	-	-	-	-	-
WHAK415-A5	1.3	0.2	55	1.1	8.0	0.9	1.7	0.5	0.1	0.0	0.3	0.2	0.1
WHAK415-A6	1.0	0.7	12	0.8	2.9	0.3	3.2	0.3	0.0	0.0	0.2	0.2	0.0
WHAK415-A7	0.8	0.5	89	3.4	5.7	0.7	2.3	0.6	0.0	0.1	0.5	0.6	0.1
WHAK415-A8	0.7	1.2	24	1.7	1.2	0.3	1.4	0.5	0.0	0.1	0.1	0.2	0.1
WHAK602	-	-	-	-	-	-	-	-	-	-	-	-	-
WHAK602A	0.8	2.9	60	1.3	2.5	0.3	0.9	0.4	0.0	0.0	0.3	0.1	0.1
WHAK602C	0.3	5.3	79	1.3	6.2	0.2	2.0	0.4	0.0	0.1	0.3	0.5	0.0
WHAK602E	0.2	7.1	82	2.4	2.1	0.3	1.5	0.1	0.0	0.1	0.1	0.1	0.1

Sample Information	**Trace Element St Dev (ppm)**								
Sample Name	Er	Tm	Yb	Lu	Hf	Ta	Pb	Th	U
WHA039D	0.1	0.1	0.2	0.0	0.5	0.1	1.2	0.5	0.3
GP115a-06	0.2	0.0	0.2	0.0	0.3	0.0	0.5	1.1	0.4
GP115a-09	0.1	0.0	0.1	0.0	0.2	0.0	1.0	0.4	0.4
GP115a-12	0.1	0.0	0.2	0.0	0.4	0.1	0.9	1.5	0.5
GP115c-14	0.3	0.0	0.2	0.0	0.3	0.1	1.6	0.5	0.5
GP115c-18	0.1	0.0	0.1	0.0	0.2	0.1	1.8	0.6	0.3
GP115c-20	0.1	0.0	0.1	0.0	0.4	0.0	1.9	0.4	0.2
WHA039A	0.2	0.0	0.2	0.0	0.4	0.1	0.8	0.8	0.3
WHA039B	0.5	0.1	0.6	0.1	0.8	0.1	2.7	6.8	0.5
WHA039C	0.1	0.0	0.2	0.0	0.8	0.2	1.4	1.4	0.4
GP107-04	0.1	0.0	0.2	0.0	0.2	0.1	0.8	0.9	0.4
WHA039E	0.5	0.0	0.4	0.1	0.9	0.1	0.6	6.0	0.3
WHA039F	0.1	0.0	0.1	0.0	0.2	0.0	0.6	1.0	0.2
WHA039G	0.1	0.0	0.1	0.0	0.3	0.0	1.0	1.5	0.3
WHA039H	0.4	0.0	0.3	0.0	0.1	0.2	0.3	0.6	0.5
WHA039I	0.2	0.1	0.2	0.0	0.3	0.1	1.7	1.2	0.5
WHA039J	0.2	0.0	0.1	0.0	0.2	0.1	1.0	0.8	0.5
WHA039K	-	-	-	-	-	-	-	-	-
WHA109A	0.1	0.0	0.2	0.0	0.1	0.1	0.9	1.1	0.1
WHA109B	0.1	0.0	0.1	0.0	0.1	0.1	0.7	0.4	0.2
WHA109C	0.1	0.0	0.1	0.0	0.1	0.0	1.6	0.3	0.5
WHA109D	0.2	0.0	0.0	0.0	0.1	0.0	0.8	0.6	0.2
WHA109E	0.1	0.0	0.2	0.0	0.1	0.0	3.9	0.3	0.2
WHA114A	0.2	0.0	0.1	0.0	0.2	0.0	0.7	0.4	0.2
WHA114B	0.2	0.0	0.1	0.0	0.3	0.1	0.7	1.2	0.3
WHA114C	0.2	0.0	0.3	0.0	0.3	0.1	1.1	1.3	0.3
WHA114D	0.2	0.0	0.3	0.0	0.3	0.1	0.6	1.7	0.4
WHAK415-A1	-	-	-	-	-	-	-	-	-
WHAK415-A3	-	-	-	-	-	-	-	-	-
WHAK415-A4	-	-	-	-	-	-	-	-	-
WHAK415-A5	0.2	0.0	0.1	0.0	0.4	0.0	0.8	2.3	0.0
WHAK415-A6	0.1	0.0	0.2	0.0	0.2	0.1	0.4	2.0	0.1
WHAK415-A7	0.3	0.1	0.5	0.1	0.3	0.1	0.4	2.6	0.5
WHAK415-A8	0.2	0.0	0.2	0.0	0.3	0.0	0.2	1.5	0.5
WHAK602	-	-	-	-	-	-	-	-	-
WHAK602A	0.1	0.0	0.2	0.0	0.2	0.0	0.4	0.6	0.2
WHAK602C	0.2	0.0	0.2	0.0	0.5	0.0	0.8	1.6	0.4
WHAK602E	0.3	0.0	0.1	0.1	0.3	0.0	1.1	1.1	0.4

Sample Information	**Magma Storage Conditions**			
Sample Name	Storage Pressure (MPa)	Storage pressure mineral assemblage	Zircon Saturation Temp (Boehnke *et al., 2013) (°C)*	Zircon Saturation Temp (Watson & Harrison, *1983) (°C)*
WHA039D	96	qtz-1feld	754	787
GP115a-06	127	qtz-2feld	700	740
GP115a-09	90	qtz-1feld	780	745
GP115a-12	115	qtz-1feld	782	747
GP115c-14	45	qtz-1feld	759	791
GP115c-18	99	qtz-1feld	750	784
GP115c-20	97	qtz-1feld	749	783
WHA039A	91	qtz-1feld	761	793
WHA039B	103	qtz-1feld	788	815
WHA039C	100	qtz-1feld	790	818
GP107-04	129	qtz-1feld	697	739
WHA039E	-	-	815	838
WHA039F	75	qtz-1feld	712	752
WHA039G	93	qtz-1feld	747	781
WHA039H	100	qtz-1feld	765	796
WHA039I	-	-	770	799
WHA039J	120	qtz-2feld	710	748
WHA039K	-	-	-	-
WHA109A	-	-	754	787
WHA109B	75	qtz-1feld	707	745
WHA109C	85	qtz-2feld	684	727
WHA109D	96	qtz-2feld	704	743
WHA109E	85	qtz-2feld	701	740
WHA114A	132	qtz-2feld	701	742
WHA114B	142	qtz-2feld	699	740
WHA114C	131	qtz-2feld	699	740
WHA114D	122	qtz-1feld	705	745
WHAK415-A1	88	qtz-2feld	-	-
WHAK415-A3	122	qtz-2feld	-	-
WHAK415-A4	120	qtz-2feld	-	-
WHAK415-A5	71	qtz-2feld	747	781
WHAK415-A6	75	qtz-1feld	730	766
WHAK415-A7	125	qtz-1feld	706	745
WHAK415-A8	97	qtz-2feld	714	753
WHAK602	-	-	-	-
WHAK602A	-	-	768	796
WHAK602C	-	-	768	795
WHAK602E	-	-	766	793